Journal of
Materials Chemistry A

ROYAL SOCIETY
OF CHEMISTRY

REVIEW

View Article Online
View Journal | View Issue

Cite this: *J. Mater. Chem. A*, 2024, **12**, 29383

Recent review on self-supported one-dimensional core/shell nanostructures based on WO_3 for enhanced electrochromism

Jiangbin Su, *[ab] Longlong Chen,*[b] Chunyan Xu,[a] Yu Liu,[b] Long Shen[b] and Zuming He[a]

Received 5th August 2024
Accepted 5th October 2024

DOI: 10.1039/d4ta05474a

rsc.li/materials-a

Self-supported one-dimensional (1D) core/shell nanostructures (SS1DCSNs) offer multiple inherent advantages in the field of electrochromism, establishing them as a prominent emerging technology. This review categorizes SS1DCSNs into self-supported 1D nanostructures and core/shell structures, providing an in-depth analysis of their various advantages in electrochromism. Tungsten trioxide (WO_3) has garnered significant attention owing to its exceptional electrochromic performance, and is considered one of the most promising materials in this domain. With integration and analysis of existing research, this review delivers a comprehensive overview of the current state of development and future research prospects of WO_3-based SS1DCSNs in electrochromism.

1. Introduction

As human society and technology continue to advance rapidly, the demand for energy is also increasing. However, the extensive use of fossil resources like coal, oil, and natural gas leads to a significant rise in greenhouse gas emissions. According to relevant statistics, building energy consumption accounts for 30–40% of the world's primary energy use.[1] It is projected that greenhouse gas emissions related to buildings will escalate to a staggering 15.6 million tons by 2030.[2] The primary uses of energy in buildings are for cooling and heating purposes in air conditioning systems, as well as for lighting appliances.[3] Windows are essential for facilitating the exchange of light and heat between buildings and the external environment. Notably, approximately 30% of the energy consumed to maintain comfortable indoor temperatures during winter and summer is lost through windows, highlighting their importance in buildings.[4]

The solar spectrum consists of various wavelengths, with the ultraviolet spectrum ($\lambda < 400$ nm) accounting for about 6.6%, the visible spectrum (400 nm $< \lambda <$ 700 nm) for about 44.7%, and the infrared spectrum ($\lambda > 700$ nm) for about 48.7%.[5,6] Rational control and utilization of solar light energy are crucial for green buildings, as they can significantly improve energy efficiency and create a more comfortable office and learning

---

[a] *Jiangxi Provincial Key Laboratory of Power Batteries & Energy Storage Materials, School of New Energy Science and Engineering, Xinyu University, Xinyu 338004, People's Republic of China. E-mail: jbsu@cczu.edu.cn*

[b] *School of Microelectronics and Control Engineering, Changzhou University, Changzhou 213159, People's Republic of China. E-mail: S22060858003@smail.cczu.edu.cn*

Jiangbin Su

Jiangbin Su received his PhD from Xiamen University in 2017. From 2008 to 2024, he served as a lecturer, associated professor, and professor at Changzhou University. Since 2024, he has been a professor at Xinyu University. His research interests include nanoscale engineering and structural instability, thin-film technology, and electrochromic materials and devices.

Longlong Chen

Longlong Chen received his BS degree from Huaide College, Changzhou University. He is currently pursuing his MS degree at the School of Microelectronics and Control Engineering, Changzhou University. His research interests primarily focus on the fabrication of metal oxide nanomaterials and multifunctional electrochromic devices.

environment.[7] Fortunately, electrochromic (EC) smart glass can change its color in response to the strength of an external electric field, dynamically adjusting the intensity of full-spectrum sunlight.[8–10] For example, it can allow visible light to pass through while blocking infrared light, ensuring both daylighting and thermal insulation.[11–14] This technology can reduce the energy consumption required to maintain comfortable temperatures in office buildings and residential homes throughout the year, while also addressing the issue of increasing urban light pollution.

Electrochromism is a fascinating phenomenon observed in materials where their optical properties, such as reflectivity, transmittance, and absorbance, undergo a stable and reversible change when subjected to an applied electric field (less than 5 V).[15,16] From a visual perspective, it refers to the materials switching between multiple colors. At the microscopic level, this involves the reversible injection and extraction of ions and electrons within these materials under the influence of the electric field.[17–19] EC materials can be broadly categorized into two groups: organic and inorganic.[20,21] Organic EC materials primarily consist of conductive polymers and bipyridine compounds such as polypyrrole (PPy),[22] polyaniline (PANI),[23] polythiophene (PEDOT),[24] polyindole (PIN),[25] and violet essence.[26] Inorganic EC materials typically include transition metal oxides and Prussian blue derivatives, such as tungsten trioxide (WO_3),[27] titanium dioxide (TiO_2),[28] nickel oxide (NiO),[29] vanadium pentoxide (V_2O_5),[30] molybdenum trioxide (MoO_3),[31] tricobalt tetraoxide (Co_3O_4),[32] niobium oxide (Nb_2O_5),[33] tantalum pentoxide (Ta_2O_5),[34] and Prussian blue (PB).[35] Significant progress has been made in the development of EC materials. Electrochromic devices (ECDs) have found practical applications in various commercial sectors. EC smart windows (Fig. 1a) are a notable example.[36] Furthermore, EC technology can be applied in various fields, including aircraft portholes (Fig. 1b),[37] automatic anti-glare rearview mirrors (Fig. 1c),[38] information display devices (Fig. 1d),[39] and smart color-changing glasses (Fig. 1e).[40]

Self-supported one-dimensional (1D) core/shell nanostructures (SS1DCSNs) offer significant advantages in enhancing material properties due to their unique geometric configurations and physicochemical characteristics.[41,42] SS1DCSNs are characterized by their 1D nanostructures, self-supported, and core/shell structures. In the case of the basic 1D nanostructures (such as nanorods, nanowires, and nanofibers), the width and thickness (or diameter in the case of cylindrical morphology) are constrained to a nanoscale range between 1 and 100 nm. In contrast, these structures are highly ductile in the lengthwise direction and can reach several micrometers or even hundreds of micrometers or millimeters.[43] The self-supported property is capable of maintaining its shape and structural stability, without the necessity for external reinforcement. This particular structure is especially conducive to the expeditious injection/extraction of ions and electrons.[44] The core/shell structures typically consist of an inner core wrapped by one or more outer shells, and both the core and shell can be constructed from the same or different materials. A heterogeneous structure can be formed between the core and shell, which can optimize chemical stability, conductivity, and other properties.

EC materials based on SS1DCSNs have been extensively developed and investigated.[45–47] Among these, WO_3 stands out as the most widely studied inorganic EC material, owing to its substantial economic and commercial potential.[48–54] Despite this, there is a notable lack of comprehensive reviews specifically focusing on SS1DCSNs based on WO_3 within the field of electrochromism. Additionally, detailed explanations of the advantages of self-supported 1D nanostructures and core/shell structures are scarce. This review aims to fill this gap by providing an in-depth analysis of the potential benefits and unique characteristics of these structures. Furthermore, it offers a thorough overview of the development of SS1DCSNs based on WO_3 in the field of electrochromism by integrating and analyzing existing studies.

2. The main factors affecting the EC performance of WO_3

WO_3 has garnered significant interest from the scientific community due to its numerous advantages, including its

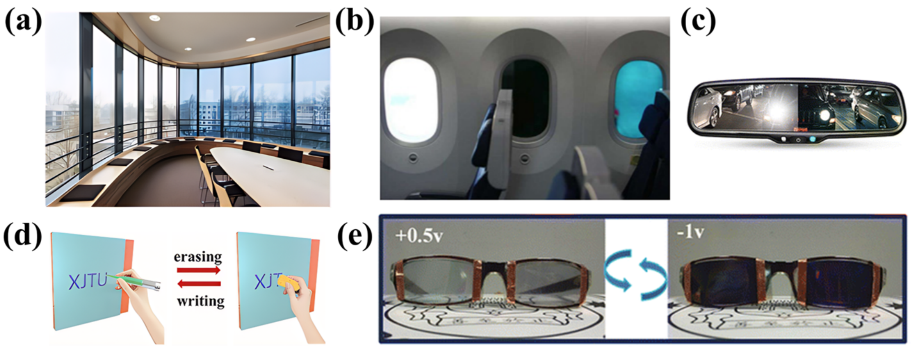

Fig. 1 (a) EC smart windows. (b) Coloring-changing aircraft portholes. (c) Automatic anti-glare rearview mirrors based on electrochromism. Reproduced from ref. 11 with permission from the Royal Society of Chemistry, Copyright 2023. (d) Information display devices based on electrochromism. Reproduced from ref. 39 with permission from the American Chemical Society, Copyright 2021. (e) Smart color-changing glasses. Reproduced from ref. 40 with permission from the Royal Society of Chemistry, Copyright 2019.

abundance, affordability, low operating voltage, and excellent EC performance.[17,36,55,56] When a cathodic voltage is applied to WO_3 films, cations and electrons are injected into the material. This causes a portion of W^{6+} to absorb electrons and be reduced to W^{5+}, resulting in the formation of tungsten bronze and transforming the films from transparent to blue. Conversely, when an anodic voltage is applied, the cations and electrons are removed from the films. This leads to the oxidation of W^{5+} back to W^{6+}, gradually bleaching the films from blue to transparent. The reaction process can be expressed by the following equation:[57–59]

$$WO_3(\text{transparent}) + xM^+ + xe^- \leftrightarrow M_xWO_3(\text{blue}) \quad (1)$$

where x denotes the number of embedded ions and M^+ represents H^+, Li^+, K^+, Na^+, *etc.*

Since the discovery of electrochromism in WO_3, extensive experimental research has been conducted to investigate its electrochemical and optical properties.[60–63] Based on extensive previous research, we have identified three crucial factors affecting the EC performance of WO_3: crystallinity, surface morphology, and conductivity.

2.1 Crystallinity

The crystallinity of WO_3 plays a crucial role in its EC properties.[64,65] Amorphous WO_3 (a-WO_3) is characterized by a disordered structure with loose stacking and random atomic configuration, featuring numerous irregular polygonal channels that enhance ion and electron transport.[66] This unique structure contributes to the exceptional optical modulation,[67] rapid switch response,[68] and high coloration efficiency of a-WO_3 films.[69] However, the inherent instability of this structure results in limited cycle life.[70] In contrast, crystalline WO_3 (c-WO_3) demonstrates improved cycling stability due to its highly ordered atomic arrangement and enhanced substrate adhesion.[71] However, the dense structure of c-WO_3 hinders ionic transport, leading to slower response time.[72]

2.2 Surface morphology

The morphological structure significantly influences the kinetics of ion insertion/extraction and the charge transfer mechanism.[59] The electrochromism in WO_3 films involves a dual injection/extraction process of ions and electrons.[58] This process can be broken down into five steps within a cycle: (1) transfer of ions from the electrolyte to the film surface; (2) penetration of ions into the film and their movement within it; (3) incorporation of ions into the WO_3 lattice; (4) removal of ions from the WO_3 lattice; and (5) exit of ions from the film. Surface properties of the film, such as porosity,[48] roughness,[73,74] and specific surface area,[55] influence the reactive sites and ion diffusion paths between WO_3 and the electrolyte.[75]

2.3 Conductivity

Conductivity is a crucial factor in the redox kinetics of WO_3 films.[76] WO_3 is a typical N-type semiconductor with a relatively low conductivity of about 10^{-4}–10^{-6} S cm^{-1}. The low conductivity results in slower migration of ions and electrons, ultimately impacting the response speed of electrochromism.[77] Additionally, low conductivity also creates a higher charge transfer energy barrier, necessitating a higher driving voltage for the charge transfer process.[78] This increased voltage consumption leads to higher energy usage and decreased energy conversion efficiency. Furthermore, low conductivity limits the maximum achievable optical density at an applied voltage, affecting the optical contrast and display quality of the films. Lastly, low conductivity may compromise the chemical stability of the materials over multiple cycles, impacting their cycle life and reliability.

Crystallinity, surface morphology, and conductivity are all significant factors that affect the EC performance of WO_3. SS1DCSNs can effectively address these issues due to their unique geometrical configurations and physicochemical properties. The following section will describe the advantages of SS1DCSNs in the field of electrochromism from two perspectives.

3. EC advantages of SS1DCSNs

3.1 Self-supported 1D nanostructures

Over the past decades, nanotechnology has proven to be an effective strategy for improving the performance of EC materials. Nanostructures can be classified into zero-dimensional (0D, such as nanodots,[79] nanoparticles[66,80]), one-dimensional (1D, such as nanorods,[81,82] nanowires,[83,84] and nanotubes[85]), two-dimensional (2D, such as nanosheets,[86] nanoplates[87]), and three-dimensional (3D, usually consisting of some special structures). Nanostructures of different dimensions exhibit distinct variations in surface morphology, porosity, roughness, and specific surface area, leading to substantial variations in the optical and electrochemical properties of the films. Among the various nanostructures, self-supported 1D nanostructures offer several advantages (see Fig. 2), such as controllable areal density of electroactive materials, strong adhesion between the substrates and electroactive materials, ease of surface modification with hybrid nanostructures, and more.[43,88]

3.1.1 Controllable areal density of electroactive materials. Electrochromism originates from the dual injection/extraction

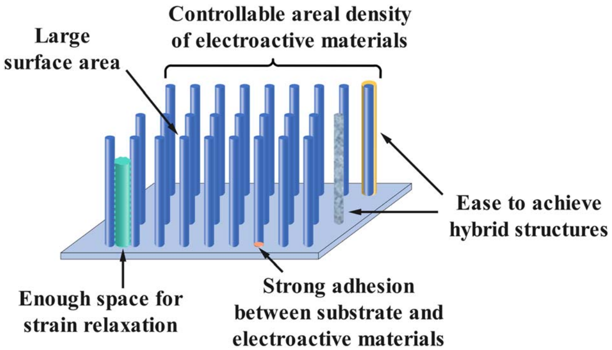

Fig. 2 Schematic diagram illustrating the advantages of an ideal self-supported 1D nanostructure for electrochromism.

of ions and electrons.[57] When accepting/extracting ions and electrons, the electroactive materials will undergo strain relaxation.[88] While a low areal density can help alleviate strain relaxation, it may also lead to an unsatisfactory optical contrast. Conversely, a high areal density can delay redox kinetics. Therefore, achieving excellent EC performance requires an optimal areal density of electroactive materials. The sufficient spacing between electroactive materials allows for strain relaxation during the reaction process, significantly improving ion transport and charge transfer.[43] Currently, the preparation methods for self-supported 1D nanostructures can be divided into two main categories: template-derived and template-free techniques.[89–91] The template-derived methods rely on replicating well-enclosed voids (such as holes, pores, channels, or other hollow spaces) within the template.[43] While this approach enables the creation of highly desirable self-supported 1D nanostructures, it also presents significant limitations due to its high cost and complexity. In contrast, most template-free techniques for synthesizing self-supported 1D nanostructured thin films are based on wet chemical methods.[7,42,54,84,92] The synthesis of self-supported 1D nanostructures with optimal surface densities can be achieved by adjusting various factors that influence hydrothermal products, such as the choice of capping agent, solvent system, temperature, and reaction time.[93] Moreover, this process is cost-effective, simple, and suitable for further investigation. All of the self-supported 1D nanostructures discussed in this review were prepared using template-free methods.

3.1.2 Strong adhesion between the substrates and electroactive materials. The synthesis techniques commonly employed for fabricating self-supported 1D nanostructured thin films involve the direct growth of electroactive materials on a substrate.[94,95] This process typically results in robust physical (or chemical) bonds between the electroactive materials and the substrate.[43] Strong adhesion ensures the structural integrity of the electrode, effectively preventing the separation of the EC materials from the substrate and promoting long-term cycling stability.

3.1.3 Improved redox kinetics. Compared to bulk or other nanostructures, self-supported 1D nanostructures exhibit improved redox kinetics.[43,95–97] These structures benefit from a rough surface morphology, offering high specific surface area and abundant open channels.[46,81,98] These features can shorten the diffusion length of ions and electrons, ensuring efficient charge transfer during the EC process. Additionally, numerous surface defects formed during preparation also significantly enhance the kinetics of redox reactions occurring at (or near) the surface.[99] This rapid redox kinetics leads to enhanced pseudocapacitive effects, beneficial for fast switch response. Enhanced surface effects have been observed in arrays of self-supported 1D nanostructures such as nanofibers,[100] nanorods,[101] and nanotubes.[102] Furthermore, delicately designed self-supported 1D nanostructures can significantly improve their ion diffusion coefficient and electrical conductivity.[99]

3.1.4 Ease of achieving hybrid structures. Most methods for fabricating self-supported 1D nanostructures are wet chemical methods. By adding liquids with different properties to the reactive precursors, phenomena such as mixed valence, new phases, defects, and structural changes in energy bands can be realized in nanostructures.[43] Self-supported 1D core/shell hybrid nanoarrays can be created by using pre-prepared self-supported 1D structural materials as a substrate and then depositing additional material onto it. These core/shell nanostructures demonstrate improved EC properties, including increased optical contrast, quicker response time, and greater coloration efficiency.[46,98] The shell materials can be the same as the core but in a different crystal phase, resulting in a crystalline-amorphous core/shell nanoarray structure.[103] However, in most cases, the shell materials are different from the core.[104]

3.1.5 Ease of integration and multifunctionality. Self-supported 1D nanostructures can be used alone or combined with other nanomaterials (such as 2D materials, nanoparticles, *etc.*) to form composite structures. The integration of such structures can further enhance EC performance and realize the fusion of multiple functions (such as photoelectric conversion, sensing, *etc.*), providing a broad platform for designing and manufacturing multifunctional intelligent ECDs.

3.2 Core/shell structures

In recent studies, core/shell structures have emerged as a promising strategy for designing functional interface systems with tunable physical and chemical properties.[7,41,42,54] Unlike straightforward mixtures of materials, core/shell structures consist of a core and a shell that are bound together by specific physical or chemical interactions, such as covalent bonds, ionic bonds, or van der Waals forces.[43] These interactions can lead to mixed valence states, the formation of new phases, defects, and modifications in the energy band structure, all of which enhance the optical absorption and electrochemical properties of EC materials.[105,106] Furthermore, core/shell structures address the limitations of single-component systems, resulting in stable, high-performance materials. When both the core and shell are composed of inorganic materials, their electronic band interactions facilitate efficient electron and ion transport, thereby enhancing redox kinetics.[107–109] If the core is inorganic and the shell is organic, the structure can display high optical contrast, color diversity, and rapid switching response due to the conductive polymer, while also maintaining chemical stability thanks to the mechanical strength of the inorganic component.[110,111] Additionally, core/shell structures allow for multifunctional integration within a layer of EC films or devices. These key advantages of utilizing core/shell structures are critical for the efficient and stable operation of EC systems.

3.2.1 Enhanced durability and cyclic stability. During the preparation of EC films, electroactive materials are typically grown directly on transparent conductive substrates (such as ITO and FTO).[81,112] When two substances with disparate crystal structures are brought into direct contact, crystal mismatch occurs due to differences in their lattice parameters (including but not limited to lattice constants, cell angles, and cell shapes).[113] This mismatch results in lattice distortion, stress concentration, and interface defects within the electroactive materials, severely degrading the chemical stability of the films and potentially leading to fracture.[114] Core/shell structures can address this issue by selecting a material with appropriate lattice matching as the core layer, which functions as a "buffer layer" between the substrate and the shell layer (electroactive materials), reducing the mismatch between crystals.[55,115–117] This design significantly reduces the generation of lattice distortion and interfacial defects, thus improving the durability and cycling stability of the EC films.

3.2.2 Optimized charge transport and ion diffusion. In core/shell structures, the core can be made of a highly conductive material, while the shell serves as the EC layer, optimizing the charge transfer process. Highly conductive materials possess lower resistivity and enhanced electron transport characteristics, allowing rapid electron distribution into the EC materials when a voltage is applied.[118,119] For cathodic (or anodic) EC materials, when a cathodic (or anodic) voltage is applied, electrons can be rapidly injected into (or extracted from) the EC materials, simultaneously attracting cations (or anions) from the electrolyte. Upon reversing the voltage, electrons can be rapidly extracted from (or injected into) the cathodic (or anodic) EC materials, causing the cations to be released (or anions to be injected). Alternatively, the core can be the EC layer, while the shell is designed for high ion diffusion, accelerating ion transfer rates. This rapid ion diffusion enables a fast color change, crucial for real-time applications like display technologies and optical modulators.

3.2.3 Controllable optical properties. The optical properties of core/shell structures can be controlled by adjusting the crystallinity, chemical composition, thickness, and interface effects of the core and shell layers.[7,42,117] Firstly, the crystallinity of EC materials directly affects their light absorption and transmission behavior.[103,120] By combining EC materials with different crystallinity, the absorption spectrum of core/shell structures in the coloring state can be tuned. For instance, the inner core can be crystalline, while the outer shell can be amorphous, allowing a range of absorptions from visible to infrared.[121–123] Secondly, the refractive index, reflectivity, and transparency of the shell materials affect issues like the refraction, reflection, and absorption of sunlight by the core/shell structure.[124,125] By adjusting the thickness and chemical composition of shell materials, light transmission, and reflection can be controlled, thereby regulating optical contrast and brightness.[41,47,111,126,127] Thirdly, the interface effect and electronic structure between the core and shell play a crucial role in the optical properties.[43] Adjusting the energy band alignment and charge transfer behavior at the core/shell interface can control the absorption and reflection properties of the EC materials, affecting the range of color change and optical contrast.[98,117] These measures allow customization of core/shell structures based on specific application requirements, providing flexibility in the fabrication of ECDs with specific color change ranges.

3.2.4 Easy of integrating multifunctional devices. Core/shell structures enable the integration of multiple functionalities within a single ECD. For example, both the electrochemical energy storage and electrochromism involve redox reactions, allowing these functions to be combined into a single film or device.[128,129] However, there is a trade-off between electrochromism and electrochemical energy storage, such as the need for high optical contrast and fast color switching, high optical modulation with low charge consumption, and faster response times, which often comes at the cost of stability due to porous structures.[74,130–132] This challenge necessitates carefully designed nanostructured morphologies. The fabrication of SS1DCSNs with high ion insertion and extraction kinetics offers an optimal solution to these issues. Additionally, ECDs with tunable multi-color properties can be prepared by integrating core/shell particles with diverse color modulation capabilitie.[92,133] Moreover, the EC function can be combined with other functionalities, such as UV blocking and thermal regulation, to achieve more intelligent applications.[41,43,134,135] By meeting multiple application requirements with a single material system, the potential uses of EC materials are significantly expanded.

3.2.5 High energy efficiency. Optimized charge transfer and ion diffusion capabilities enable dual diffusion of ions and electrons at low voltages, reducing energy losses during oxidation-reduction.[116,117] This allows core/shell structures to exhibit higher energy conversion efficiency, significant for achieving low-power EC technology.

4. SS1DCSNs based on WO_3

4.1 Self-supported 1D nanostructures

For basic 1D nanostructures, such as nanorods and nanowires, the width and thickness (or diameter in the case of cylindrical morphology) are constrained to the nanoscale range of 1 to 100 nm. In contrast, these structures are highly ductile along their length, extending to several micrometers, hundreds of micrometers, or even millimeters.[43] Their self-supporting nature allows them to maintain shape and structural stability without external reinforcement. These characteristics are particularly advantageous for the rapid injection and extraction of ions and electrons during the EC process, thereby enhancing the performance of the films.[44]

Ma *et al.* fabricated vertically aligned WO_3 nanorod arrays (with a diameter of about 80 nm) using a template-free hydrothermal technique, adjusting the ratio of deionized water to acetonitrile (1 : 1) and employing urea as a directing agent (see Fig. 3a).[93] These self-supported 1D nanostructures, with their high specific surface area and numerous ion transport channels, exhibit excellent properties, including lager optical contrast ($\Delta T = 66\%$ at 632.8 nm) (see Fig. 3b), short response time ($t_c = 6.7$ s, $t_b = 3.4$ s) (see Fig. 3c), and high coloration efficiency (CE = 106.8 $cm^2\ C^{-1}$) in the visible light region. Similarly, Cai *et al.* produced the vertically aligned hierarchical WO_3 nano-architectures on FTO-coated substrates using a solvothermal method.[95] Various nanostructures (such as nanoclusters, nanotrees, and nanowires) were achieved by modulating the concentration of HCl in the precursor solution. For example, adding 20 μL of HCl resulted in a uniform and well-aligned WO_3 nanowire array with an average diameter of 20 nm and a length of approximately 1.1 μm (see Fig. 3d). These self-supported nanowire arrays demonstrated favorable

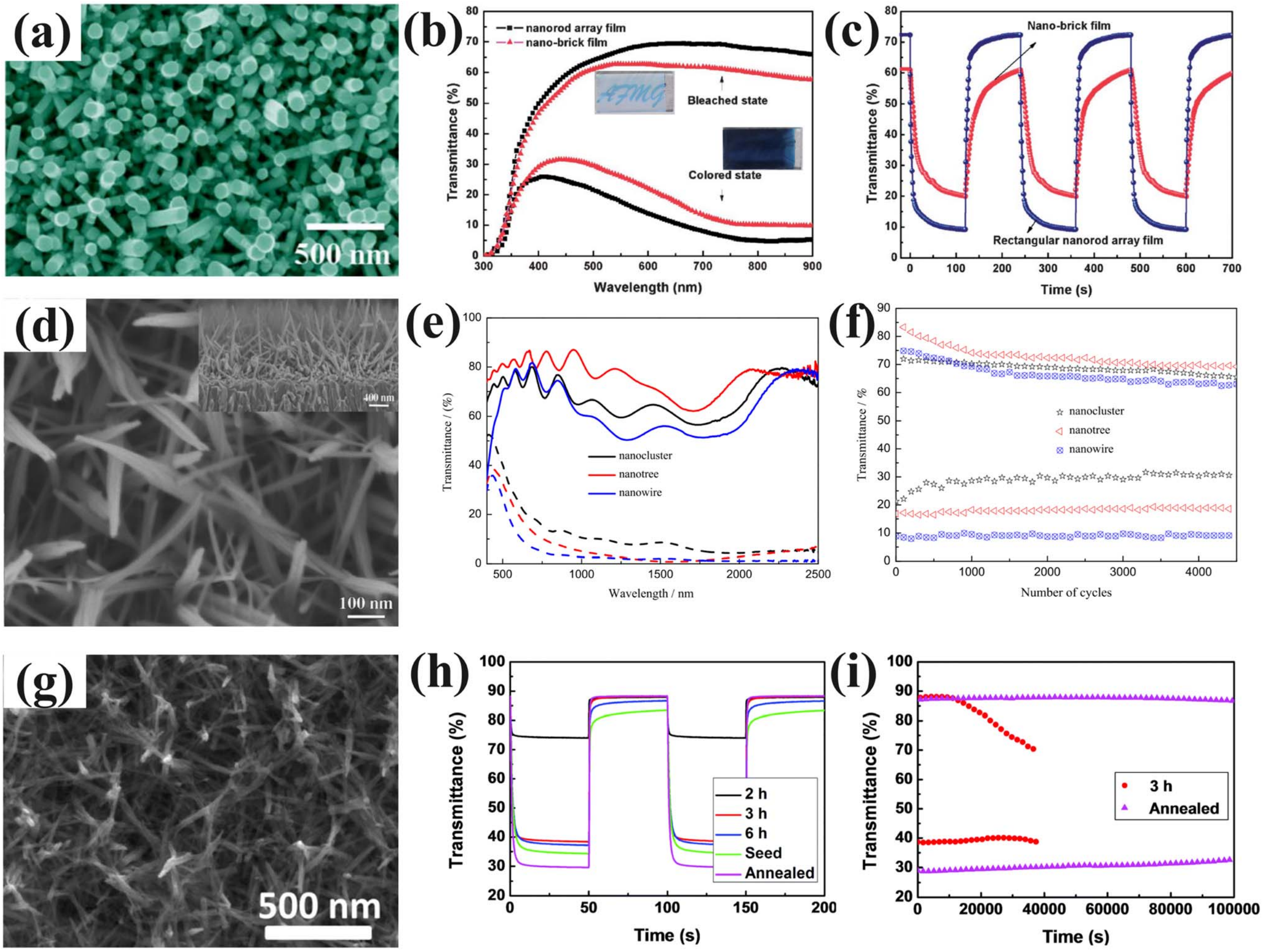

Fig. 3 (a) FE-SEM images of WO_3 nanorods synthesized in deionized water–acetonitrile solvent with a 1 : 1 volume ratio. (b) Transmittance spectra at an applied voltage of ±2.0 V. (Insets) Digital photos of the colored and bleached states. (c) Switching time characteristics between the colored and bleached states, measured at 632.8 nm with an alternating potential of ±2 V. Reprinted from ref. 93 with permission from the Royal Society of Chemistry, Copyright 2013. (d) SEM image of WO_3 nanowires prepared using 20 μL of HCl. (e) Visible and near-infrared transmittance spectra in the colored and bleached states (solid curves: bleached state; dashed curves: colored state). (f) Durability test over 4500 cycles at a wavelength of 633 nm within a potential range of −0.7 to 1.0 V. Reprinted from ref. 95 with permission from Elsevier, Copyright 2014. (g) SEM image of the 3 h WO_3 nanowire film after annealing at 400 °C in N_2. (h) *In situ* optical responses of the 3 h WO_3 nanowire film after annealing at 400 °C in N_2. (i) Stability test of the WO_3 nanowire films before and after annealing at 400 °C in N_2. Reprinted from ref. 136 with permission from the Royal Society of Chemistry, Copyright 2016.

performance, including lager optical contrast ($\Delta T = 66\%$ at 633 nm, $\Delta T = 53.9\%$ at 2000 nm) (see Fig. 3e), fast switching response ($t_c = 2.0$ s, $t_b = 3.4$ s), and high coloration efficiency (CE = 120 $cm^2\ C^{-1}$). Li *et al.* demonstrated the deposition of WO_3 nanowire thin films directly onto bare FTO substrates *via* a solvothermal method, eliminating the need for an a-WO_3 seed layer.[136] The average diameter of WO_3 nanowires was 20 nm. Following annealing in N_2 at 400 °C, the morphology of the WO_3 nanowires remained unaltered (see Fig. 3g). However, their cycling stability increased by almost tenfold. (see Fig. 3i) Additionally, the optical modulation of the film was enhanced from 49.82% to 58.69%, while maintaining consistent response time ($t_c = 0.76$ s, $t_b = 2.68$ s) (see Fig. 3h) and coloration efficiency (CE = 61.89 $cm^2\ C^{-1}$).

Self-supported 1D nanostructures have demonstrated a significant improvement in the performance of WO_3 thin films compared to their dense structural counterparts. However, certain challenges remain that must be addressed to further enhance their functionality and expand their applications. A key issue is the limited color-changing range of these self-supported 1D nanostructures, which typically shifts only between transparent and blue. This restricted chromatic diversity hinders their potential for broader development. Additionally, the optical modulation capabilities of these structures are mainly confined to the visible spectrum, limiting their use in wider EC applications. These limitations can be effectively addressed by employing SS1DCSNs, which provide a promising approach to extending both the color range and optical modulation capabilities beyond the visible spectrum, thereby expanding their practical applications across various advanced technologies. The various properties and characteristics of WO_3-based SS1DCSNs are summarized in Table 1.

4.2 SS1DCSNs with WO_3 Shell

4.2.1 ZnO/WO_3 core/shell. One of the major drawbacks of WO_3 is its low electrical conductivity, which limits its applications in ECDs.[140] To address this issue, Bi *et al.* employed magnetron sputtering to deposit a layer of AZO (Al-doped ZnO) on PET substrate prior to the synthesis of ZnO/WO_3 core/shell nanoarrays (see Fig. 4a).[119] Al, as a donor element, can improve the carrier concentration and electron transport properties of ZnO.[141] As a result, the ZnO/WO_3 core/shell nanoarrays demonstrate a lower driving voltage. Meanwhile, the ZnO nanowires acted as a porous template for depositing the WO_3 layer, resulting in core/shell nanoarrays with a rougher surface morphology and numerous open channels (see Fig. 4b). This structure can significantly amplify the electroactive area and facilitate the diffusion of Li^+ ions during the electrochemical process.[142–144] Consequently, the ZnO/WO_3 core/shell nanostructure exhibits wide optical contrast ($\Delta T = 68.2\%$ at 633 nm) (see Fig. 4c), fast response time ($t_c = 2.8$ s, $t_b = 6.2$ s), and high coloration efficiency (CE = 80.6 $cm^2\ C^{-1}$) (see Fig. 4d) in the visible light region.

4.2.2 TiO_2/WO_3 core/shell. In most cases, electroactive materials are typically directly grown on transparent conductive substrates such as ITO and FTO. However, a crystal phase difference between the electroactive materials and the substrates leads to a phenomenon known as crystal mismatch, which can significantly degrade the chemical stability of the films and potentially cause them to fracture.[113] In response to this issue, researchers have introduced the concept of a "buffer layer". This layer effectively alleviates the crystal mismatch phenomenon, reduces lattice distortion and interfacial defects, and ultimately enhances the durability and cycling stability of films.[115]

Cai *et al.* synthesized self-supported 1D rutile TiO_2 (r-TiO_2) nanorods on FTO substrates using a hydrothermal method prior to the deposition of WO_3 films.[137] Both TiO_2 nanorods and FTO are rutile-type with the same lattice structure, minimizing the probability of crystal mismatch. The cycling durability of SS1DCSNs can be guaranteed. Additionally, by varying the electrodeposition time, three types of samples, TiO_2@200WO_3, TiO_2@400WO_3, and TiO_2@600WO_3 were prepared, exhibiting distinct optical properties under the full solar spectrum. For instance, TiO_2@200WO_3 shows exceptional optical contrast in the near-infrared region ($\Delta T = 70.3\%$ at 1800 nm), while TiO_2@600WO_3 exhibits excellent optical transmittance in the visible light region ($\Delta T = 57.2\%$ at 750 nm). TiO_2@400WO_3 combines the advantages of both, with balanced optical properties in the visible light and near-infrared regions ($\Delta T = 52.2\%$ at 750 nm; $\Delta T = 46.3\%$ at 1800 nm; $\Delta T = 37.2\%$ at 10 μm).

Aside from the commonly observed SS1DCSNs, the scientific community has also explored numerous core/shell structures with unique configurations. For example, Zhao *et al.* synthesized a novel hexagonal WO_3/oriented TiO_2 nanorods arrays (h-WO_3/TiO_2 NRA) through a simple two-step hydrothermal process (see Fig. 5a).[55] In this structure, the r-TiO_2 nanorods (radial dimension of 40 nm) acted as "scaffolds" for the

Table 1 EC performance parameters and characteristics of WO_3 films based on SS1DCSNs

Sample	Microstructure	ΔT	t_c/t_b (s)	Color changing	Reference
ED-WO_3	Dense structure	73.06% (632.8 nm)	22/14	Transparent and blue	76
B-WO_3	Dense structure	43.8% (776 nm)	15.2/35.3	Transparent and blue	51
CN-2	Nanorods	66% (632.8 nm)	6.7/3.4	Transparent and dark blue	93
WO_3 nanowires	Nanowires	66% (633 nm)	3.4/2.0	Transparent and dark blue	95
WO_3/ZnO	SS1DCSNs	68.2% (633 nm)	2.8/6.2	Transparent and dark blue	119
TiO_2@400WO_3	SS1DCSNs	52.2% (750 nm), 46.3% (1800 nm)	4.6/3.2	Transparent and dark blue	137
h-WO_3/TiO_2 NRAs	SS1DCSNs	73.45% (633 nm)	6.6/2.0	Transparent and dark blue	55
TW	SS1DCSNs	61.9% (800 nm)	10/10	Transparent and dark blue (self-repairable)	138
TWNT	SS1DCSNs	76.2% (633 nm)	7.2/2.3	Transparent and dark blue (self-repairable)	114
c-WO_3/15a-WO_3	SS1DCSNs	84.5% (633 nm), 80.0% (1500 nm)	3.6/1.2	Transparent and dark blue	139
WO_3 NWs/NPs	SS1DCSNs	87.1% (633 nm), 75.5% (1300 nm)	2.8/1.9 (bright to cold) 6.9/2.7 (bright to dark)	Transparent, pale blue, and dark blue	46
WO_3/15 min-TiO_2	SS1DCSNs	85.3% (633 nm), 87% (1500 nm)	3.0/1.1	Transparent and dark blue	42
WO_3/1cir-V_2O_5	SS1DCSNs	57% (776 nm)	4.8/4.3	Black, green-yellow, and orange-yellow	126
PB@WO_3	SS1DCSNs	35.14% (633 nm), 60.55% (1200 nm), and 67.18% (1800 nm)	0.5/0.5 (PW to PB) 0.7/0.5 (PB to PG)	PW, PB, and PG	98
WO_3/PANI	SS1DCSNs	59% (700 nm)	3.4/2.2 (purple to blue) 4.8/2.2 (light yellow to blue)	Dark blue, light yellow, green, and royal purple	110
WO_3/PEDOT	SS1DCSNs	72% (633 nm)	3.8/3.6	Pale blue and dark blue	127
P6ICA/WO_3	SS1DCSNs	55% (625 nm)	0.72/0.91	Dark green, yellow, and yellow-green	133

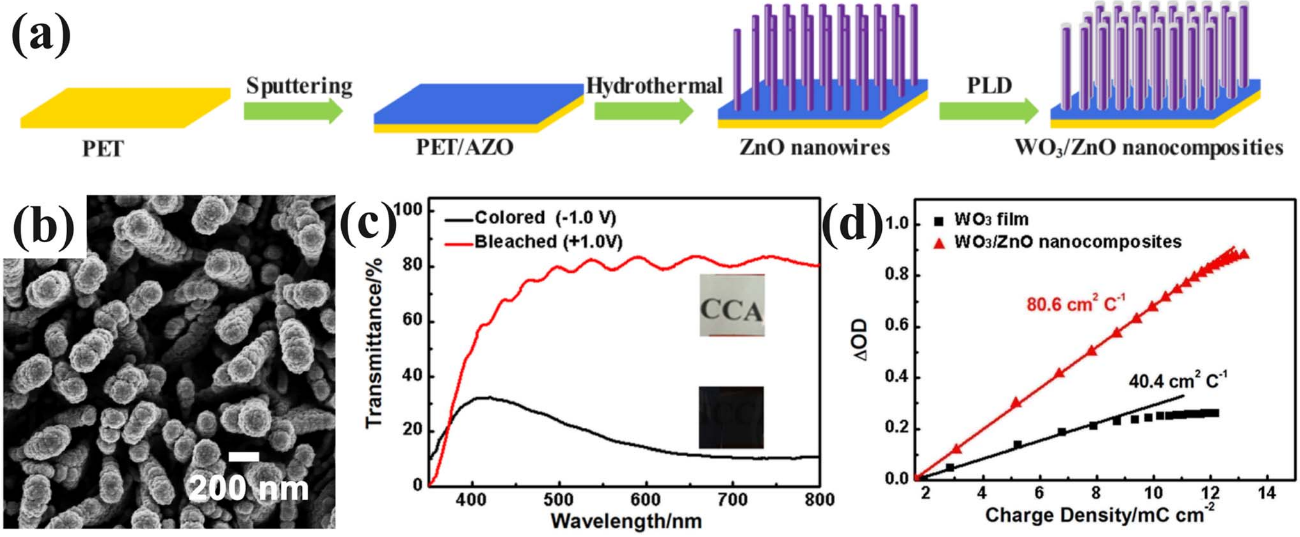

Fig. 4 (a) Schematic diagram of the formation process of WO_3/ZnO nanocomposites. (b) SEM image of WO_3/ZnO nanocomposites. (c) Transmittance spectra of WO_3/ZnO nanocomposites. (Insets) Digital photos in colored and bleached states. (d) The coloration efficiency of WO_3/ZnO nanocomposites at 633 nm. Reprinted from ref. 119 with permission from Royal Society of Chemistry, Copyright 2019.

subsequent growth of h-WO_3 (radial size from 20 to 100 nm), forming a new type of partially interpenetrating structure with high porosity (see Fig. 5b). This structure reduces the ion diffusion path length and facilitates the electrolyte penetration and ion diffusion process. As a result, the h-WO_3/TiO_2 NRA demonstrates significant transmittance modulation (ΔT = 73.45% at 633 nm) (see Fig. 5c) and switching response (t_c = 6.6 s, t_b = 2.0 s). At the same time, the r-TiO_2 acts as a "buffer layer" between the substrate and the h-WO_3, and its strong adhesion to the two materials ensures exceptional cyclic stability, with a retention rate of 92.9% in optical contrast after 2000 cycles (see Fig. 5d).

Huo *et al.* synthesized another novel r-TiO_2/h-WO_3 nanorod array (TW) using the same process (see Fig. 5e).[138] TW is based on r-TiO_2 nanorods (radial dimension of 65 nm), and h-WO_3 nanorods (radial diameter from 25 to 55 nm) are grown along the surface of the substrate material in specific orientations (see Fig. 5f). In addition to the strong adhesion between the electroactive materials and the FTO substrates, TW also possesses a very high specific surface area and a large number of gaps. It can exhibit well-balanced performance (see Fig. 5g), including optical modulation in the visible region (ΔT = 61.9% at 800 nm), response time (t_c = 10 s, t_b = 10 s), coloration efficiency (CE = 153 cm^2 C^{-1}), and cycling stability (optical contrast decreases by only 2% after 2000 cycles).

Inspired by the tree-strengthening approach, Zhao *et al.* devised a novel nanostructure known as TiO_2 nanorod-reinforced WO_3 nanotree (TWNT) architecture.[114] In this design, r-TiO_2 nanorods (radial dimension of 40 nm) serve as the "trunk" while WO_3 nanowires, featuring a plethora of active sites, intertwine as the "branches" atop the r-TiO_2 nanorods (see Fig. 5h and i). Leveraging the robust stability of r-TiO_2 nanorods and the high specific surface area and abundant interstitial spaces provided by the WO_3 nanowire branches, TWNT exhibits significantly enhanced redox kinetics. Compared to solitary WO_3 nanotrees, TWNT thin films demonstrate exceptional EC performance, including substantial optical modulation (ΔT = 76.2% at 633 nm) (see Fig. 5j), swift response time (t_c = 7.2 s, t_b = 2.3 s) (see Fig. 5k), high coloration efficiency (CE = 125.6 cm^2 C^{-1}), and captivating cycling stability, with an optical contrast retention rate of 77.35% after 10 000 cycles (see Fig. 5l).

4.3 SS1DCSNs with WO_3 core

4.3.1 Crystalline/amorphous WO_3 core/shell. The crystallinity of WO_3 significantly influences its light absorption and transmission properties.[92,103,120] This behavior stems from the different coloration mechanisms in amorphous and crystalline forms. The coloration in a-WO_3 is due to small polaron absorption,[145] where electrons and Li ions are injected simultaneously into the film. Electrons are confined to W^{5+} sites, while Li ions are located at the center of the [WO_6] octahedron or bound to interstitial oxygen atoms, creating spatial separation between ions and electrons and forming small polarons.[146] These polaritons enable photon energy absorption, oscillating between adjacent W^{5+} and W^{6+} sites.[103] Conversely, the coloration mechanism in crystalline WO_3 resembles the Drude-mode of free electrons, where injected electrons are not confined to W^{5+} positions but act as free electrons,[147] leading to a transition from a semiconductor to a metalloid state. This distinct EC mechanism results in a-WO_3 and c-WO_3 exhibiting varied absorption and reflection across the solar spectrum.

SS1DCSNs leverage the advantages of both amorphous and crystalline forms. Tang *et al.* synthesized crystalline/amorphous WO_3 core/shell nanostructure using solvothermal and magnetron sputtering methods (see Fig. 6a).[139] The core consists of 1D h-WO_3 nanowire arrays, and the shell is a-WO_3 (see Fig. 6b), with shell thickness controlled by sputtering time. The c-WO_3/15a-WO_3 core/shell structure shows large optical modulation

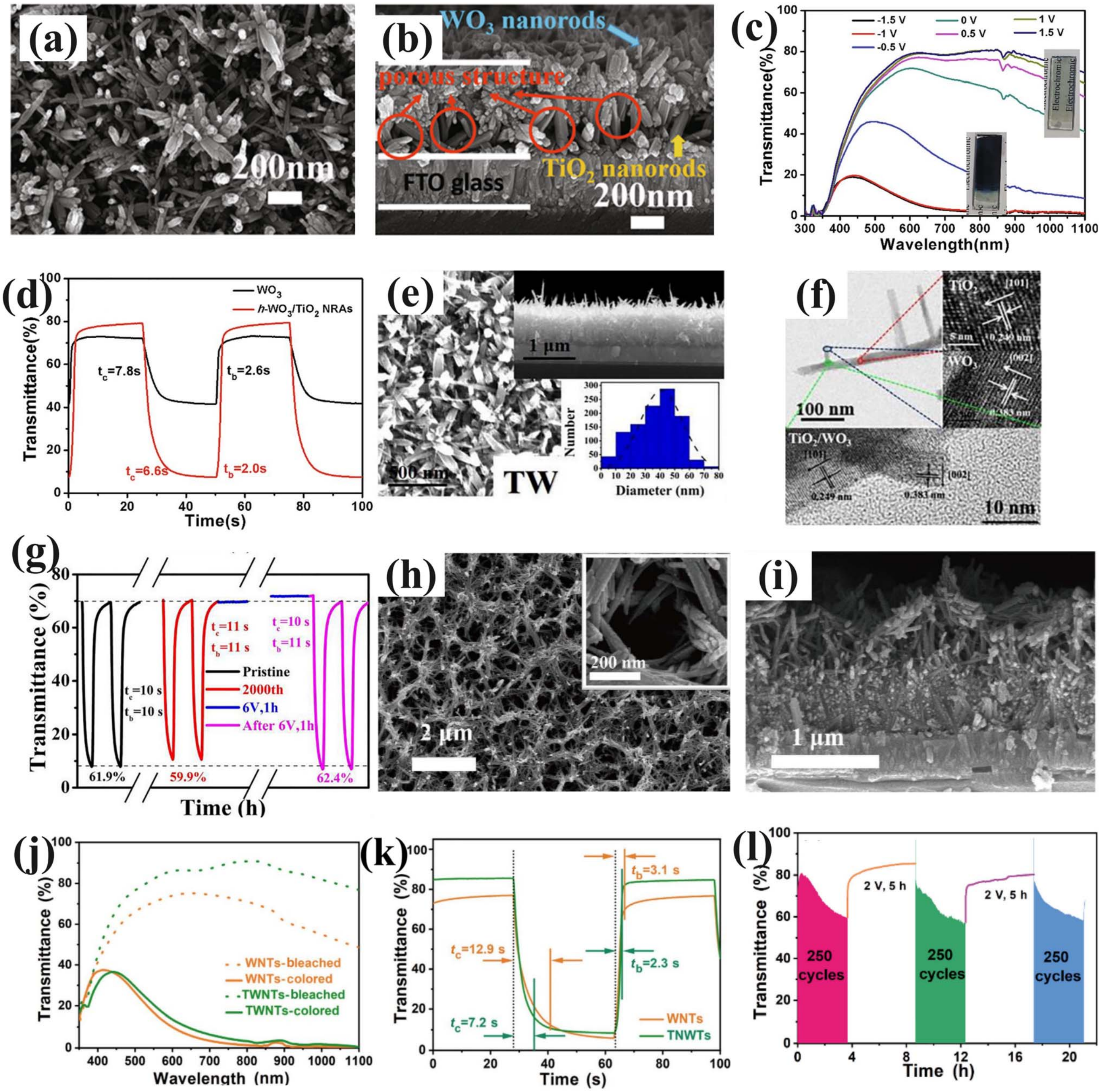

Fig. 5 (a) SEM image of h-WO_3/TiO_2 NRAs. (b) Cross-sectional view of h-WO_3/TiO_2 NRAs. (c) Transmittance of h-WO_3/TiO_2 NRAs under various potentials. (Inserts) Digital photos of h-WO_3/TiO_2 NRAs in colored and bleached states. (d) *In situ* transmittance response curves at 633 nm under an alternating potential of ±1 V for 2000 cycles. Reproduced from ref. 55 with permission from Elsevier, Copyright 2021. (e) Top and cross-sectional view SEM images and diameter statistics of sample TW. (f) TEM image of single TiO_2 and WO_3 nanorods in sample TW. (g) Optical modulation and response time of TW in its pristine, 2000th and de-tapping states. Reproduced from ref. 138 with permission from Elsevier, Copyright 2022. (h) SEM image of TWNTs film. (Insets) High-magnification image. (i) Cross-sectional view of TWNTs film. (j) Transmittance spectra at the voltage of ±1 V. (k) *In situ* transmittance spectra at 633 nm under an alternating potential of ±1 V. (l) *In situ* transmittance spectra at 633 nm at the voltage of ±1 V for 35 s each. Reproduced from ref. 114 with permission from Springer Link, Copyright 2022.

($\Delta T = 84.5\%$ at 633 nm; $\Delta T = 80.0\%$ at 1500 nm) in both visible and near-infrared regions (see Fig. 6c), with a short response time ($t_b = 1.2$ s, $t_c = 3.6$ s) and excellent cycling stability (91.9% optical contrast retention after 3000 cycles).

Similarly, Liu *et al.* developed porous WO_3 films with nanowires/nanoparticles (WO_3 NWs/NPs) core/shell architecture (see Fig. 6d).[46] This structure, with amorphous WO_3 nanoparticles uniformly grown on triclinic WO_3 nanowires, exhibits three modes: cool, dark, and light (see Fig. 6e and f). In the "bright" mode (0.5 V), the films exhibit high transmittance for solar irradiance, blocking only 5.9% of near-infrared heat and 12.2% of visible light. In the "cold" mode

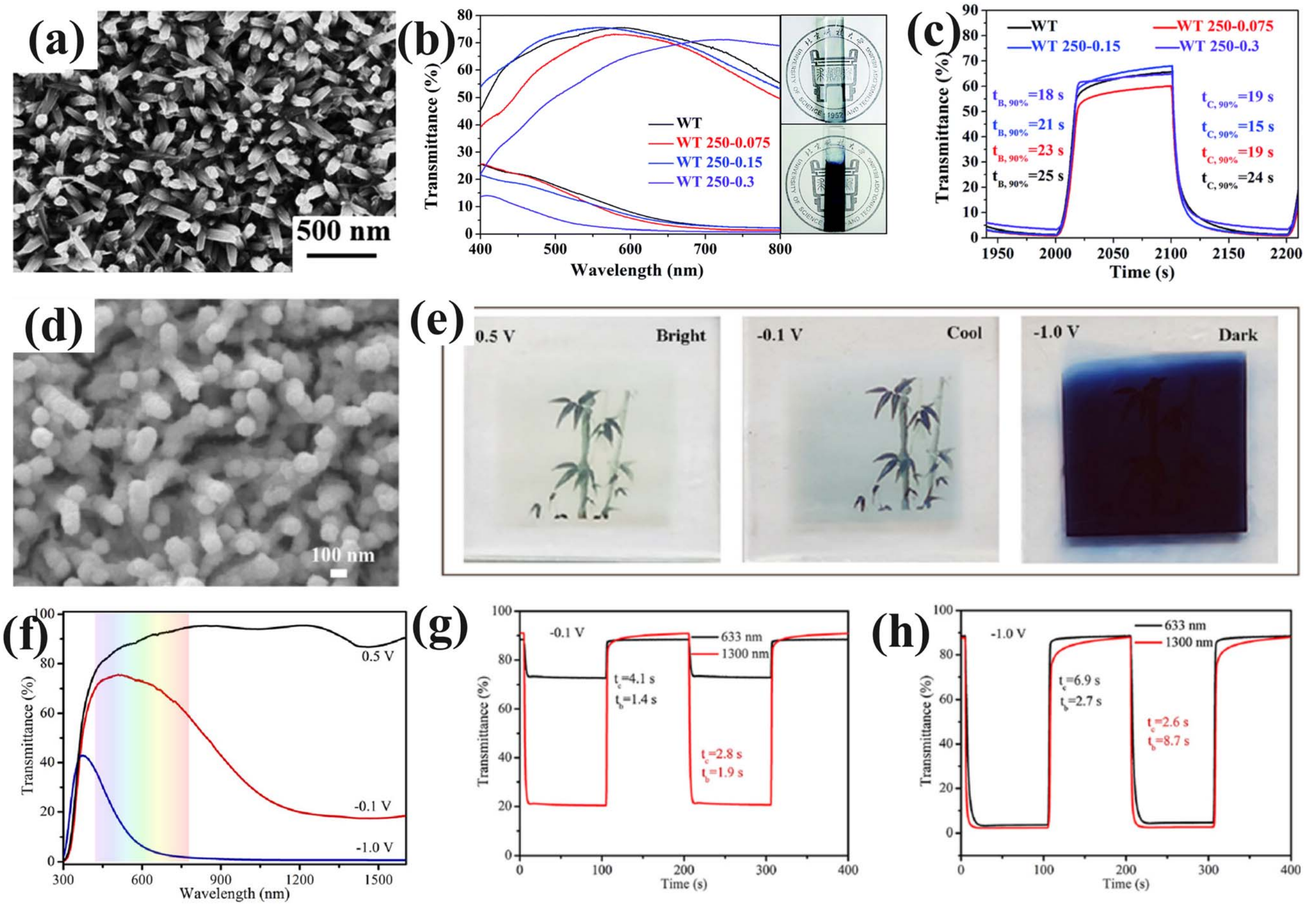

Fig. 6 (a) SEM image of c-WO_3/15a-WO_3 core/shell nanowires. (b) HRTEM images of c-WO_3/15a-WO_3 core/shell nanowires. (Inset) High magnification image of the interface between the crystalline core and amorphous shell. (c) The transmittance of c-WO_3/15a-WO_3 core/shell nanowires. (Insets) Switch response curve and digital photos. Reproduced from ref. 139 with permission from Elsevier, Copyright 2019. (d) SEM image of the WO_3 NWs/NPs film. (e) Digital photos in the "bright" (0.5 V), "cool" (−0.1 V), and "dark" (−1.0 V) modes. (f) Transmittance spectra of WO_3 NWs/NPs film. (g) *In situ* transmittance response spectra at 633 nm and 1300 nm under an alternating potential of 0.5 V and −0.1 V. (h) *In situ* transmittance response spectra at 633 nm and 1300 nm under an alternating potential of 0.5 V and −1.0 V. Reproduced from ref. 46 with permission from American Chemical Society, Copyright 2023.

(−0.1 V), the films block 66.1% of near-infrared heat while maintaining 70.8% visible light transmittance. In the "dark" mode (−0.5 V), the films block 99.0% of near-infrared heat and 87.3% of visible light, providing privacy and reducing heat near buildings. These films also demonstrate fast response times (see Fig. 6g and h) and stable cycling performance.

4.3.2 WO_3/TiO_2 core/shell. In SS1DCSNs, the chemical composition and thickness of the shell material are crucial as they affect both macroscopic properties (refraction, reflection, and absorption of sunlight) and microscopic properties (energy band alignment and charge transfer behavior).[121–125] Tang *et al.* created a WO_3/TiO_2 core/shell nanostructure using solvothermal and magnetron sputtering techniques (see Fig. 7a).[42] The core consists of 1D h-WO_3 nanowire arrays, with an anatase TiO_2 shell (see Fig. 7b), the thickness of which can be controlled by sputtering time. The WO_3/15 min-TiO_2 core/shell structure exhibits optimal optical contrast ($\Delta T = 85.3\%$ at 633 nm; $\Delta T = 87\%$ at 1500 nm) in both visible and near-infrared regions (see Fig. 7c), along with excellent response time ($t_b = 1.1$ s, $t_c = 3.0$ s) (see Fig. 7d), coloration efficiency (CE = 102.1 cm^2 C^{-1}), and cycling stability (95.6% optical contrast retention after 3000 cycles). These properties are attributed to the increased contact area between the electroactive material and the electrolyte,[148,149] the energy band structure modification due to the WO_3/TiO_2 heterostructure,[13] the reduction of contact resistance by W–O–Ti bonds,[150] and the prevention of Li-ion capture inside the WO_3 film.[49]

Shen *et al.* synthesized core/shell hexagonal phase tungsten oxide/amorphous titanium dioxide nanorod arrays (WTNRA) on FTO substrates using hydrothermal and spin coating methods.[47] They investigated the effects of the TiO_2 shell on the microstructure and properties of WTNRA arrays by varying the TiO_2 precursor concentration. At an optimal precursor concentration of 0.050 mol L^{-1}, the WTNRA films exhibited a loose and porous structure (see Fig. 7e), facilitating electrolyte penetration, and showed excellent optical modulation ($\Delta T = 78\%$ at 682 nm) (see Fig. 7f), fast switching response ($t_b = 12$ s, t_c

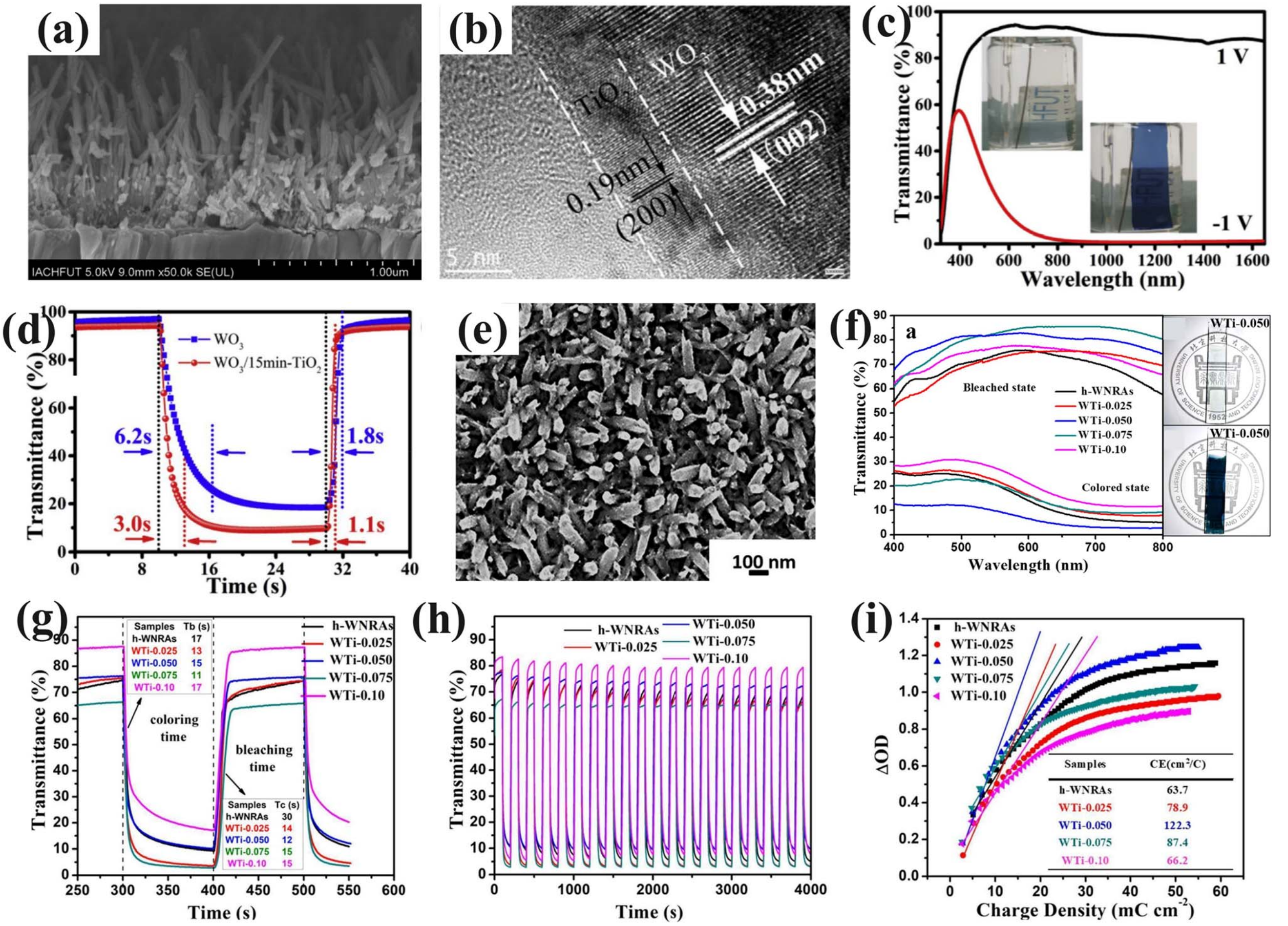

Fig. 7 (a) SEM image of WO_3/15 min-TiO_2 core/shell nanowires. (b) HRTEM image of a WO_3/15 min-TiO_2 core/shell nanowire. (c) Transmittance spectra of WO_3/15 min-TiO_2 core/shell nanowires. (Insets) Digital photos in colored and bleached states. (d) *In situ* coloration and bleaching switching responses for WO_3/TiO_2 core/shell nanowires at 633 nm at a voltage of ±1 V. Reproduced from ref. 42 with permission from Elsevier, Copyright 2019. (e) SEM image of WTi-0.050. (f) Transmittance spectra of samples prepared using different concentrations of TiO_2 spin-coating solution at a voltage of ±3 V. (Insets) Digital photos of WTi-0.050 at colored and bleached states. (g) Transmittance curves and switching time between colored and bleached states at 800 nm. (h) *In situ* transmittance curves of obtained samples with different concentrations of TiO_2 spin-coating solution. (i) Optical density *vs.* charge density of samples with different concentrations of TiO_2 spin-coating solution. Reproduced from ref. 47 with permission from Elsevier, Copyright 2020.

= 15 s) (see Fig. 7g), good cycling stability (see Fig. 7h), and high coloration efficiency (CE = 122.3 $cm^2\ C^{-1}$) (see Fig. 7i).

4.3.3 WO_3/V_2O_5 core/shell.

Tang *et al.* reported a novel WO_3 nanorod arrays decorated with V_2O_5 dots (see Fig. 8a).[126] Initially, vertically oriented WO_3 nanorod arrays were grown on FTO using a thermal solvent method, with the diameter of the WO_3 nanorods decreasing gradually from the base (80 nm) to the tip (30 nm). Subsequently, WO_3/*X*cir-V_2O_5 (where *X* represents the number of potential cycles) nanorod array films were prepared by electro-deposition at a scanning rate of 50 mV s^{-1} within a potential range of 0 V to 2.7 V. The size and distribution density of the V_2O_5 particles were precisely controlled by varying the potential width and the number of potential cycles. Microstructural characterization confirmed the presence of V_2O_5 dots with an average diameter of less than 3 nm on the surface of the WO_3/1cir-V_2O_5 nanorod array (see Fig. 8b and c).

V_2O_5 is unique among transition metal oxides for possessing both cathodic and anodic EC properties. When a cathodic voltage was applied, both V_2O_5 and WO_3 exhibited a synergistic effect, resulting in simultaneous coloration, and the films displayed a black color at −1 V due to the superposition of the two colors (see Fig. 8d). In contrast, when an anodic voltage was applied, only V_2O_5 undergoes coloration. Depending on the extent of the reaction, the films can exhibit two colors: green-yellow (0.6 V) and orange-yellow (1.5 V) (see Fig. 8d). The *in situ* transmittance curves of WO_3/V_2O_5 films at 776 nm were measured by applying square wave voltages of −1.0 V (for 30 s) and 1.5 V (for 30 s). The results showed that the films have good response times ($t_b = 4.4$ s, $t_c = 4.8$ s) and high coloration efficiency (CE = 87.1 $cm^2\ C^{-1}$). Although the optical contrast is relatively average ($\Delta T = 57\%$), the color versatility could allow these films to be used in a wider range of applications.

4.3.4 WO_3/PB core/shell.

Meng *et al.* first developed the concept of coating PB on WO_3 nanorods to create inorganic–organic core/shell structures (WO_3/PB).[151] WO_3 and PB

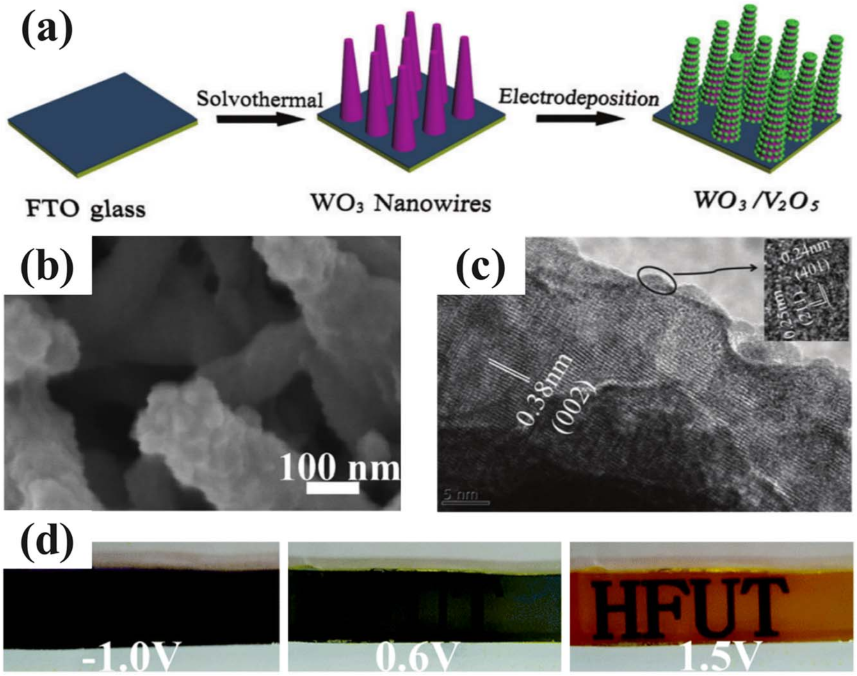

Fig. 8 (a) Schematic diagram of the formation process of WO_3/V_2O_5 films. (b) SEM image of the WO_3/1cir-V_2O_5 films. (c) HRTEM image of the WO_3/1cir-V_2O_5 films. (Inset) HRTEM image of the V_2O_5 nanoparticles on the WO_3 nanorod. (d) Digital photos of the WO_3/1cir-V_2O_5 films measured at voltages of −1.0 V, 0.6 V, and 1.5 V. Reproduced from ref. 126 with permission from Royal Society of Chemistry, Copyright 2018.

represent two distinct EC materials with differing polarities, forming an electron donor–acceptor pair system between them. The ion diffusion coefficients of the WO_3/PB core/shell structure are substantially enhanced compared to single WO_3 and PB films (over 7 times higher than PB films and 35% higher than bare WO_3 films). Additionally, the optical modulation (ΔT = 61% at 500 nm) and coloration efficiency (CE = 142.8 $cm^2\ C^{-1}$) of the WO_3/PB films were significantly improved.

Zhao *et al.* prepared a porous 1D WO_3 nanorod-modified PB (PB@WO_3) (see Fig. 9a and b).[98] WO_3, with its relatively narrow bandgap and suitable electron density, effectively addresses these drawbacks of PB. Moreover, the exceptional optical modulation capability of WO_3 in the near-infrared region allows PB@WO_3 to exhibit excellent dual-frequency modulation ability (ΔT = 35.14% at 633 nm; ΔT = 60.55% at 1200 nm; ΔT = 67.18% at 1800 nm). Meanwhile, the presence of PB enables PB@WO_3 to display three distinctive colors (see Fig. 9c): PW (−0.2 V), PB (0.6 V), and PG (1.2 V), offering a broader range of options for practical applications. The stable porous structure of the 1D nanorods and the electron interactions between WO_3 and PB contribute to a very short state switching time for PB@WO_3 (0.5 s/0.5 s for coloring/bleaching from PW to PB; 0.7 s/0.5 s for coloring/bleaching from PB to PG) (see Fig. 9d and e) and good cycling stability (the current density did not exhibit obvious changes after 1000 cycles) (see Fig. 9f).

4.3.5 WO_3/PANI core/shell. Organic EC materials have demonstrated notable advantages, including faster switching response times (within 1 s) and a wide range of colors (blue, green, violet, *etc.*). However, one of the most significant challenges faced by organic EC materials is their poor stability and durability over extended periods of use. In contrast, inorganic EC materials offer prominent chemical and thermal stability, allowing them to withstand harsh environmental conditions and repetitive cycling without significant degradation. It is evident that SS1DCSNs can combine the advantages of both these materials.

Cai *et al.* fabricated WO_3/PANI core/shell nanowire arrays using a combination of solvothermal and electropolymerization methods (see Fig. 10a).[110] Unlike other core/shell nanostructures, WO_3/PANI consists of WO_3 nanoclusters vertically aligned on an FTO substrate. These nanoclusters are composed of a large number of radial nanowires with tapered tips, with diameters of approximately 20 nm and lengths of around 450 nm. The external PANI shell was electrodeposited using cyclic voltammetry at a scanning rate of 50 mV s^{-1} within a potential range of 0.2 V to 1.3 V in a mixed solution of aniline and sulfuric acid. WO_3 and PANI are polarity-opposite EC materials (WO_3 is a cathodic EC material, while PANI is an anodic EC material). The separation of electrochemical activity within the applied potential window allows for a double EC reaction to occur without any loss of electrical activity. As a result, WO_3/PANI core/shell nanowire arrays can exhibit multiple EC properties, such as dark blue (−0.7 V), light yellow (−0.2 V), green (0.2 V), and royal purple (1.0 V) (see Fig. 10b and c). Additionally, the coloration/bleaching speed between the different states is excellent (t_c = 3.4 s, t_b = 2.2 s between the royal purple and light yellow; t_c = 4.8 s, t_b = 2.2 s between the dark blue and light yellow).

4.3.6 WO_3/PEDOT core/shell. Shi *et al.* reported a core/shell nanorod array of WO_3/PEDOT fabricated using solvothermal

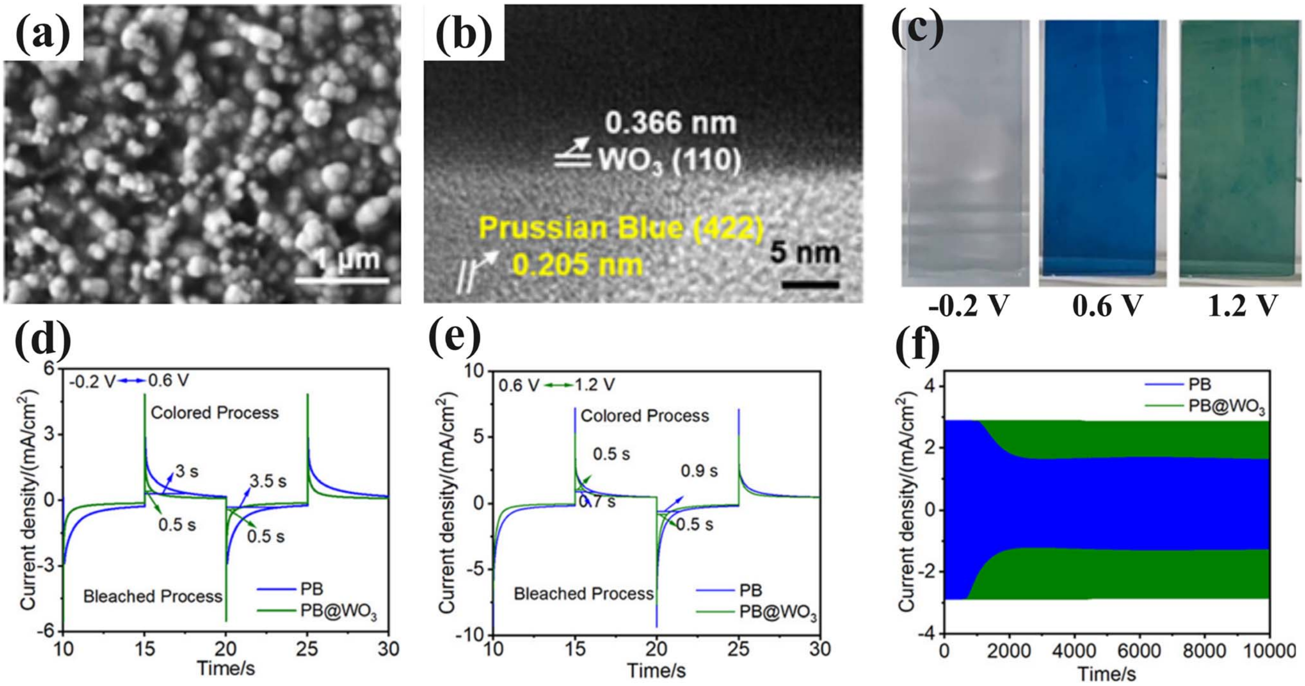

Fig. 9 (a) SEM image of PB@WO_3 film. (b) HRTEM image of PB@WO_3 film. (c) Digital photos of the PB@WO_3 film at different voltages. (d) Coloration/bleaching time between PW and PB. (e) Coloration/bleaching time between PB and PG. (f) Electrochemical stability of PB@WO_3 films at a voltage of −0.2 and 0.6 V for 1000 cycles. Reproduced from ref. 98 with permission from American Chemical Society, Copyright 2023.

and *in situ* electro-polymerization techniques.[127] The experimental results show that the core/shell nanoarrays consist of h-WO_3 nanocores wrapped in thin amorphous PEDOT nanoshells (see Fig. 11a). WO_3, acting as an electron acceptor, interacts with p-doped conjugated polymers like PEDOT, forming donor–acceptor pairs that enhance the interaction at the inorganic/

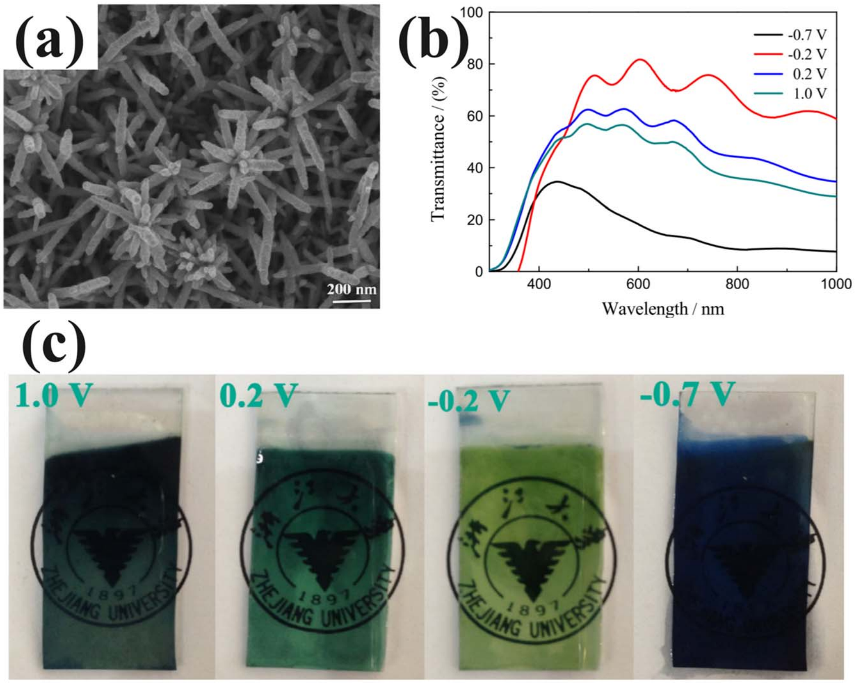

Fig. 10 (a) SEM image of WO_3/PANI core/shell nanowire array. (b) Transmittance spectra of WO_3/PANI films under different applied potentials. (c) Digital photos of WO_3/PANI core/shell nanowire array sample under different applied potentials. Reproduced from ref. 110 with permission from Elsevier, Copyright 2013.

organic interface. Compared to bare WO_3 nanorods, the optical contrast of WO_3/PEDOT core/shell nanorod arrays is slightly reduced (ΔT from 80% to 72% at 633 nm). However, their response speed is significantly improved, with coloration time reduced from 12.4 s to 3.8 s and bleaching time from 7.6 s to 3.6 s. Additionally, to meet various practical application requirements, the color depth and optical contrast of the core/shell nanorod arrays can be adjusted by modulating the applied voltage and the deposition thickness of the PEDOT nano-shell (see Fig. 11b and c).

4.3.7 WO_3/PIN core/shell nanostructure.

Li *et al.* successfully prepared WO_3/poly (indole-6-carboxylic acid) (P6ICA) nanocomposites with a core/shell structure using a simple electrodeposition-assisted hydrothermal process (see Fig. 12a).[133] Microstructural characterization shows good ionic or covalent bonding between the W atoms in WO_3 and the N atoms in P6ICA, and the energy bands of WO_3 and P6ICA are closely matched. This significantly reduces the charge transfer resistance of the WO_3/P6ICA nanocore/shell structure ($R_{ct} = 2.2\ \Omega$) and enhances ion and electron transfer rates. The WO_3/P6ICA films can achieve multiple color variations: dark green at −0.3 V, yellow at 0.0 V, and yellow-green at 0.9 V (see Fig. 12b).

Additionally, asymmetric ECDs were fabricated using WO_3/P6ICA as the positive electrode and PEDOT as the negative electrode. These WO_3/P6ICA//PEDOT devices exhibit different colors at various potentials: yellow-green at 0.0 V and blue-black at 1.4 V (see Fig. 12c). They demonstrate good optical modulation ($\Delta T = 55\%$ at 625 nm) and cycling stability, with only an 8% decrease in optical contrast after 3000 cycles, in the visible region. Although the transmittance of the WO_3/P6ICA//PEDOT devices is less than 60% in the bleached state, their short response times ($t_c = 0.72$ s, $t_b = 0.91$ s) are still remarkable (see Fig. 12d).

This section provides an overview of the literature on WO_3-based SS1DCSNs, highlighting the roles of WO_3 as both an outer shell and a core layer material. When used as the outer shell, WO_3 primarily functions as the EC layer. The inner core is typically composed of a material with high conductivity, such as AZO, which effectively reduces the driving voltage, accelerates the reaction rate, and improves energy utilization efficiency. Additionally, selecting materials with suitable crystal structures for the core layer, such as TiO_2, can significantly mitigate the crystal mismatch between WO_3 and the substrate, thereby enhancing the overall stability and performance of SS1DCSNs. When WO_3 is used as the core layer, it can serve as a porous template for depositing shell materials with a high specific surface area. If the shell material has unique optoelectronic properties (such as a-WO_3 or TiO_2), the SS1DCSNs can achieve dual-band modulation in the visible and near-infrared light regions. Furthermore, a dual EC effect can be realized if the shell material is also an EC material. WO_3 can only switch between transparent and blue states during the EC reaction, limiting its color change and applicability to specific scenarios. However, by depositing another EC material (such as V_2O_5, PB, PANI, or PIN) onto the WO_3 surface, a dual EC effect can be achieved, expanding the applicability of SS1DCSNs to various scenarios. These strategies significantly enhance the

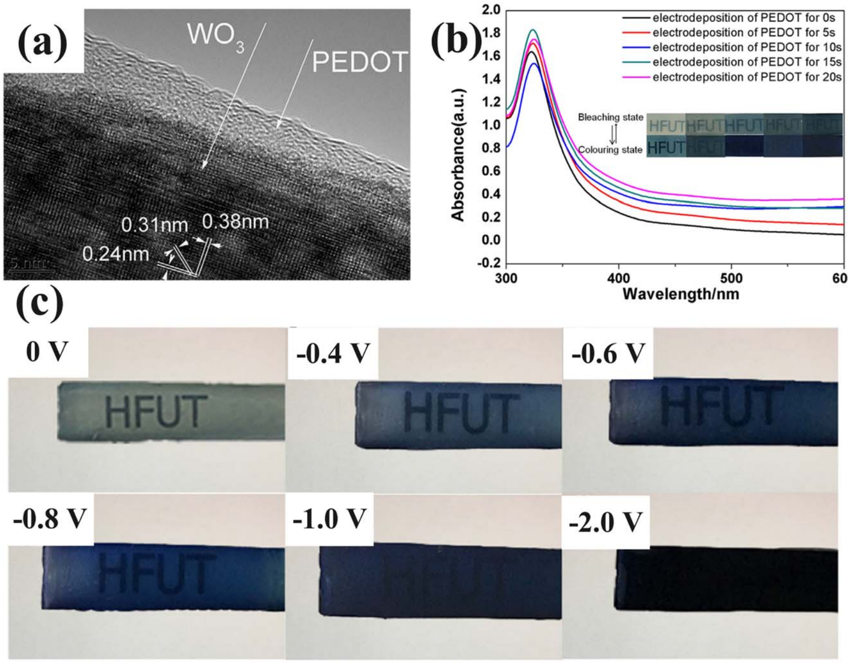

Fig. 11 (a) TEM images of WO_3/PEDOT core/shell nanorod arrays. (b) UV-absorption spectrum of WO_3/PEDOT core/shell nanorod arrays with different deposition times from 0 s to 20 s. (Insets) Optical images of samples with different deposition times (left to right: 0 s, 5 s, 10 s, 15 s, and 20 s). (c) Digital photos of WO_3/PEDOT core/shell nanorod arrays at different voltages. Reproduced from ref. 127 with permission from Elsevier, Copyright 2018.

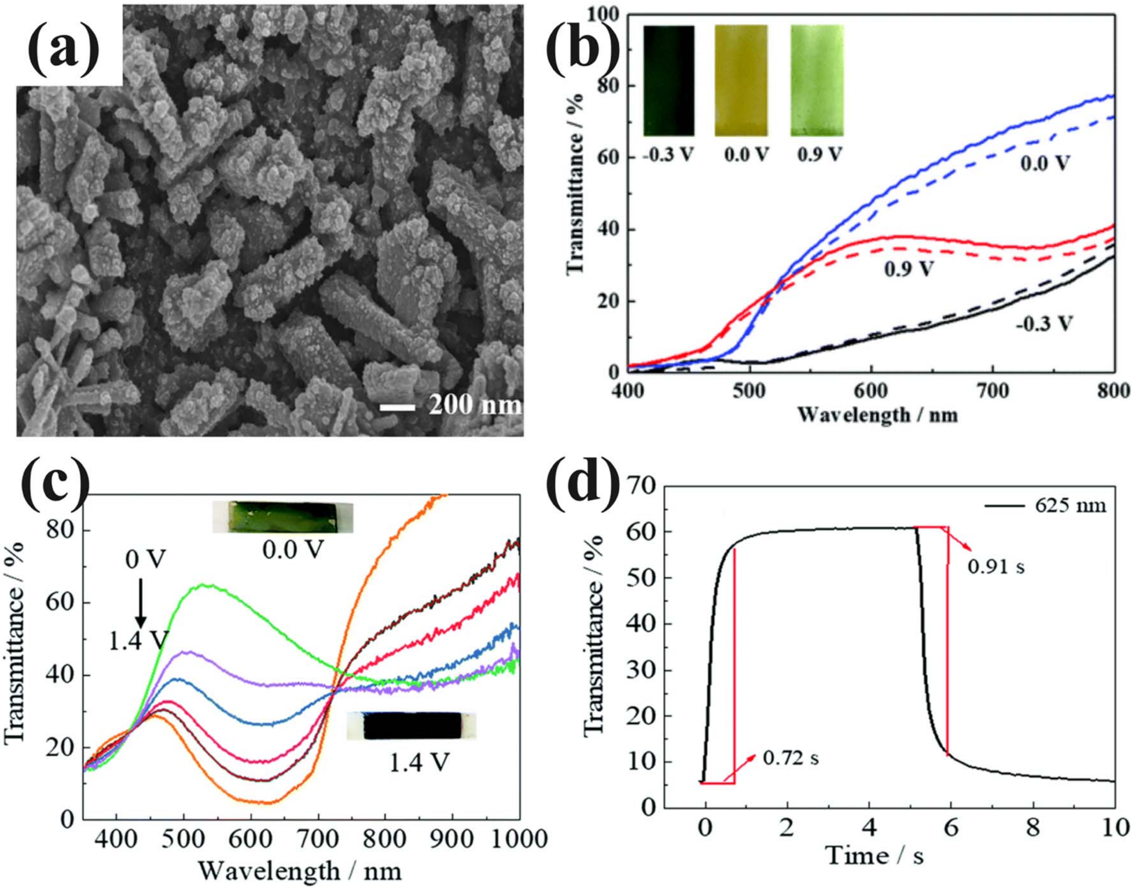

Fig. 12 (a) SEM image of P6ICA/WO_3 nanocomposites. (b) Transmittance spectra and digital photos of P6ICA/WO_3 nanocomposites under different voltages. (c) Transmittance spectra of the P6ICA/WO_3//PEDOT device under 0 to 1.4 V. (Insets) Digital photos of the device under 0.0 V and 1.4 V. (d) *In situ* transmittance response curve of P6ICA/WO_3//PEDOT device at 625 nm. Reproduced from ref. 133 with permission from Royal Society of Chemistry, Copyright 2020.

adaptability and functionality of WO_3-based SS1DCSNs, making them a promising approach to improve electrochromism.

5. Summary and outlook

SS1DCSNs have emerged as prominent technology in the field of electrochromism due to their unique geometric configurations and physicochemical properties. There has been rapid development and significant achievements in the various morphologies and materials of SS1DCSNs for enhanced electrochromism. This review provides a detailed elaboration on the advantages of these structures in the electrochromic field from two perspectives: core/shell structures and self-supported 1D nanostructures. WO_3 is one of the most widely investigated inorganic EC materials in the scientific community. ECDs based on WO_3 films, such as smart windows, automatic anti-glare rearview mirrors, smart AR glasses, and information display devices, have now found widespread applications across various fields. This review integrates and deeply analyzes the latest advancements in SS1DCSNs with WO_3 as the core or shell in recent years. Although SS1DCSNs have many advantages in the field of electrochromism, there are still some shortcomings that need to be improved.

5.1 Optimization of structural design and preparation methods

The design of SS1DCSNs and the optimization of fabrication methods are crucial for their development. The core of SS1DCSNs is composed of nanowires, nanorods, or nanotubes. Currently, there are two main approaches to synthesizing these self-supported 1D nanostructures: template-derived and template-free methods. The former relies on the replication of porous templates (such as holes, pores, channels, and other hollow spaces). The precursor is simply filled into the voids of a porous template, and after subsequent processing and template removal, the ideal self-supported 1D nanostructures can be obtained. However, the preparation of porous templates is complex and extremely costly, making it unsuitable for large-scale industrial synthesis. In contrast, the latter does not require a specific porous template. Most template-free synthesis methods for self-supported 1D nanostructures are seed layer-assisted solvothermal methods. Compared to porous templates, a seed layer is easier to prepare and less costly, and the synthesized self-supported 1D nanostructures also possess all the advantages of the former. However, its drawback is that the synthesis does not result in strictly ideal self-supported 1D nanostructures; the nanowires (or nanorods) do not grow perpendicular to the substrate, and there may be some interconnected structures. In the future, researchers need to focus on optimizing the preparation of self-supported 1D nanostructures, seeking low-cost methods that can synthesize strictly ideal self-supported 1D nanostructures.

5.2 Combination of multifunctionality and high performance

In the field of electrochromism, the future development focus of SS1DCSNs is on achieving the perfect integration of multifunctionality and high performance by introducing various functional materials and structural adjustments. For instance, by integrating photosensitive materials (such as TiO_2, Ag_2S, *etc.*) into the outer shell, it is possible to create a response to light signals, thus developing a new type of photo-controlled EC system. This system can change its color or transparency when exposed to light of a specific wavelength, making it suitable for smart windows, privacy protection, and other applications. Similarly, incorporating thermosensitive materials (such as poly(*N*-isopropylacrylamide), PNIPAM) into the shell can achieve thermally controlled electrochromism. These structures are sensitive to temperature changes and can change color by adjusting the temperature, suitable for temperature sensing and self-regulating temperature systems. Moreover, adding magnetic or conductive materials (such as ferrites, graphene, *etc.*) into the shell layer can enable a response to electromagnetic fields. Such novel structures can change color or optical properties under the influence of electromagnetic fields and can be used for information encryption, security markings, and other fields.

5.3 Ensuring structural integrity

While SS1DCSNs offer numerous advantages in the field of electrochromism, they also face issues that affect their structural integrity. (1) Over time, there may be physical or chemical mismatches at the interface between the core and shell, which can lead to stress concentrations within the core/shell structures, resulting in delamination or interfacial failure. (2) Self-supported 1D nanostructures may be extremely sensitive to mechanical stress. When subjected to external forces, they are susceptible to fracture or deformation. (3) During the EC process, self-supported 1D nanostructures may not maintain structural integrity due to redox reactions. The dimensions of the self-supported 1D nanostructures change, and this dimensional change will affect the properties of the material. In the future, researchers need to address these problems by focusing on material selection, surface modification, structural optimization, and improving synthesis methods to minimize the impact of external and internal environments on the structural integrity of SS1DCSNs.

5.4 Expansion of application fields and commercialization

SS1DCSNs are continuously expanding in the field of electrochromism (such as smart windows, information storage, and displays) and have achieved partial commercialization. It is expected that in the future, SS1DCSNs will find broader applications in smart glasses, high-resolution displays, optical sensing, and security authentication, among other areas. Commercialization is a significant trajectory in the field of electrochromism, where researchers need to further drive the development of self-supported 1D core/shell nanostructure technology. Self-supported 1D core/shell nanotechnology needs to transcend the confines of the laboratory and advance towards marketization to fulfill the practical application demands.

Data availability

No primary research results, software or code have been included and no new data were generated or analyzed as part of this review.

Conflicts of interest

There are no conflicts to declare.

Acknowledgements

This work was financially supported by the Natural Science Foundation of Jiangsu Province (BK20191453) and the Research and Innovation Program for Graduate Students of Jiangsu Province (SJCX23_1596 and KYCX23_3173).

References

1 C. G. Granqvist, M. A. Arvizu, İ. B. Pehlivan, H.-Y. Qu, R.-T. Wen and G. A. Niklasson, *Electrochim. Acta*, 2018, **259**, 1170–1182.

2 P. Singh, *J. Energy, Environ. Carbon Credits*, 2012, 61–67.

3 H. Khandelwal, A. P. Schenning and M. G. Debije, *Adv. Energy Mater.*, 2017, **7**, 1602209.

4 Q. Wang, S. Cao, Q. Meng, K. Wang, T. Yang, J. Zhao and B. Zou, *Mater. Horiz.*, 2023, **10**, 960–966.

5 T. J. Richardson, J. L. Slack and M. D. Rubin, *Electrochim. Acta*, 2001, **46**, 2281–2284.

6 S. Zhang, S. Cao, T. Zhang, Q. Yao, A. Fisher and J. Y. Lee, *Mater. Horiz.*, 2018, **5**, 291–297.

7 D. Zhou, D. Xie, F. Shi, D. Wang, X. Ge, X. Xia, X. Wang, C. Gu and J. Tu, *J. Colloid Interface Sci.*, 2015, **460**, 200–208.

8 G.-f. Cai, J.-p. Tu, C.-d. Gu, J.-h. Zhang, J. Chen, D. Zhou, S.-j. Shi and X.-l. Wang, *J. Mater. Chem. A*, 2013, **1**, 4286–4292.

9 J. Wang, L. Zhang, L. Yu, Z. Jiao, H. Xie, X. W. Lou and X. Wei Sun, *Nat. Commun.*, 2014, **5**, 4921.

10 C. Ramana, S. Utsunomiya, R. Ewing, C. Julien and U. Becker, *J. Phys. Chem. B*, 2006, **110**, 10430–10435.

11 J. Y. Zheng, Q. Sun, J. Cui, X. Yu, S. Li, L. Zhang, S. Jiang, W. Ma and R. Ma, *Nanoscale*, 2023, **15**, 63–79.

12 H. Wei, X. Yan, Y. Li, H. Gu, S. Wu, K. Ding, S. Wei and Z. Guo, *J. Phys. Chem. C*, 2012, **116**, 16286–16293.

13 G.-f. Cai, X.-l. Wang, D. Zhou, J.-h. Zhang, Q.-q. Xiong, C.-d. Gu and J.-p. Tu, *RSC Adv.*, 2013, **3**, 6896–6905.

14 Z. Shao, A. Huang, C. Cao, X. Ji, W. Hu, H. Luo, J. Bell, P. Jin, R. Yang and X. Cao, *Nat. Sustain.*, 2024, **7**, 796–803.

15 S. Deb, *Appl. Opt.*, 1969, **8**, 192–195.

16 P. R. Somani and S. Radhakrishnan, *Mater. Chem. Phys.*, 2003, **77**, 117–133.

17 L. Chen, X. Zhu, Y. Liu, L. Yang, J. Su, Z. He and B. Tang, *Electrochim. Acta*, 2024, **475**, 143644.

18 A. Lusis, J. Kleperis and E. Pentjušs, *J. Solid State Electrochem.*, 2003, **7**, 106–112.

19 G. A. Niklasson and C. G. Granqvist, *J. Mater. Chem.*, 2007, **17**, 127–156.

20 J. Guo, H. Jia, Z. Shao, P. Jin and X. Cao, *Acc. Mater. Res.*, 2023, **4**, 438–447.

21 H. Jia, X. Cao and P. Jin, *J. Inorg. Mater.*, 2020, **35**, 511–524.

22 G. E. Demir, M. Yıldırım, U. Cengiz and İ. Kaya, *React. Funct. Polym.*, 2015, **97**, 63–68.

23 J.-H. Kang, Y.-J. Oh, S.-M. Paek, S.-J. Hwang and J.-H. Choy, *Sol. Energy Mater. Sol. Cells*, 2009, **93**, 2040–2044.

24 S. I. Cho, W. J. Kwon, S.-J. Choi, P. Kim, S.-A. Park, J. Kim, S. J. Son, R. Xiao, S.-H. Kim and S. B. Lee, *Adv. Mater.*, 2005, **17**, 171–175.

25 G. Nie, L. Zhou, Q. Guo and S. Zhang, *Electrochem. Commun.*, 2010, **12**, 160–163.

26 S. Y. Choi, M. Mamak, N. Coombs, N. Chopra and G. A. Ozin, *Nano Lett.*, 2004, **4**, 1231–1235.

27 L. Pan, Q. Han, Z. Dong, M. Wan, H. Zhu, Y. Li and Y. Mai, *Electrochim. Acta*, 2019, **328**, 135107.

28 A. Ghicov, S. P. Albu, J. M. Macak and P. Schmuki, *Small*, 2008, **4**, 1063–1066.

29 S. Pereira, A. Gonçalves, N. Correia, J. Pinto, L. Pereira, R. Martins and E. Fortunato, *Sol. Energy Mater. Sol. Cells*, 2014, **120**, 109–115.

30 K. Takahashi, Y. Wang and G. Cao, *Appl. Phys. Lett.*, 2005, **86**, 053102.

31 K. i. Machida and M. Enyo, *J. Electrochem. Soc.*, 1990, **137**, 1169.

32 X. Xia, J. Tu, J. Zhang, X. Huang, X. Wang, W. Zhang and H. Huang, *Electrochem. Commun.*, 2008, **10**, 1815–1818.

33 C. Yu, D. Ma, Z. Wang, L. Zhu, H. Guo, X. Zhu and J. Wang, *Ceram. Int.*, 2021, **47**, 9651–9658.

34 C. G. Granqvist, *Sol. Energy Mater. Sol. Cells*, 2012, **99**, 1–13.

35 V. D. Neff, *J. Electrochem. Soc.*, 1978, **125**, 886.

36 G. T. Phan, D. Van Pham, R. A. Patil, C.-H. Tsai, C.-C. Lai, W.-C. Yeh, Y. Liou and Y.-R. Ma, *Sol. Energy Mater. Sol. Cells*, 2021, **231**, 111306.

37 K. Ahmad and H. Kim, *ACS Sustainable Chem. Eng.*, 2023, **11**, 10746–10754.

38 J. Zhang, J. Tu, X. Xia, Y. Qiao and Y. Lu, *Sol. Energy Mater. Sol. Cells*, 2009, **93**, 1840–1845.

39 W. Wu, H. Fang, H. Ma, L. Wu, Q. Wang and H. Wang, *ACS Appl. Mater. Interfaces*, 2021, **13**, 20326–20335.

40 Y. Wang, Z. Meng, H. Chen, T. Li, D. Zheng, Q. Xu, H. Wang, X. Y. Liu and W. Guo, *J. Mater. Chem. C*, 2019, **7**, 1966–1973.

41 T. Ghosh, L. Bansal, S. Kandpal, C. Rani, D. K. Rath, B. Sahu, S. Chhoker and R. Kumar, *J. Energy Storage*, 2023, **72**, 108640.

42 K. Tang, Y. Zhang, Y. Shi, J. Cui, X. Shu, Y. Wang, Y. Qin, J. Liu, H. H. Tan and Y. Wu, *Electrochim. Acta*, 2020, **330**, 135189.

43 Z. Tong, S. Liu, X. Li, J. Zhao and Y. Li, *Nanoscale Horiz.*, 2018, **3**, 261–292.

44 R. S. Devan, R. A. Patil, J. H. Lin and Y. R. Ma, *Adv. Funct. Mater.*, 2012, **22**, 3326–3370.

45 Y. Chen, X. Li, Z. Bi, X. He, X. Xu and X. Gao, *Electrochim. Acta*, 2017, **251**, 546–553.

46 H. Liu, Y. Zhang, P. Lei, J. Feng, S. Jia, J. Huang, C. Hu, C. Bian and G. Cai, *ACS Appl. Mater. Interfaces*, 2023, **15**, 23412–23420.

47 W. Shen, X. Huo, M. Zhang and M. Guo, *Appl. Surf. Sci.*, 2020, **515**, 146034.

48 A. Hasani, Q. Van Le, T. P. Nguyen, K. S. Choi, W. Sohn, H. W. Jang and S. Y. Kim, *Electrochim. Acta*, 2018, **283**, 1195–1202.

49 J. Han, K.-w. Ko, S. Sarwar, M.-s. Lee, S. Park, S. Hong and C.-h. Han, *Electrochim. Acta*, 2018, **278**, 396–404.

50 W. Wei, Z. Li, Z. Guo, Y. Li, F. Hou, W. Guo and A. Wei, *Appl. Surf. Sci.*, 2022, **571**, 151277.

51 Q. Xu, Y. Yin, T. Gao, G. Cao, Q. Chen, C. Lan, F. Li and C. Li, *J. Alloys Compd.*, 2020, **829**, 154431.

52 D. Ma, T. Li, Z. Xu, L. Wang and J. Wang, *Sol. Energy Mater. Sol. Cells*, 2018, **177**, 51–56.

53 Y. Li, W. A. McMaster, H. Wei, D. Chen and R. A. Caruso, *ACS Appl. Nano Mater.*, 2018, **1**, 2552–2558.

54 T. Hao, S. Wang, H. Xu, X. Zhang, J. Xue, S. Liu, Y. Song, Y. Li and J. Zhao, *Chem. Eng. J.*, 2021, **426**, 130840.

55 L. Zhao, X. Huang, G. Lin, Y. Peng, J. Chao, L. Yi, X. Huang, C. Li and W. Liao, *Chem. Eng. J.*, 2021, **420**, 129871.

56 Z. Shao, A. Huang, C. Ming, J. Bell, P. Yu, Y.-Y. Sun, L. Jin, L. Ma, H. Luo and P. Jin, *Nat. Electron.*, 2022, **5**, 45–52.

57 Q. Zhao, Y. Fang, K. Qiao, W. Wei, Y. Yao and Y. Gao, *Sol. Energy Mater. Sol. Cells*, 2019, **194**, 95–102.

58 M. Wang, Y. Chen, B. Gao and H. Lei, *Adv. Electron. Mater.*, 2019, **5**, 1800713.

59 R.-T. Wen, C. G. Granqvist and G. A. Niklasson, *Nat. Mater.*, 2015, **14**, 996–1001.

60 J. Su, X. Zhu, L. Chen, Y. Liu, H. Qi, Z. He and B. Tang, *Electron. Mater. Lett.*, 2024, **20**, 131–139.

61 X. Zhu, H. Qi, J. Chen, J. Su, Z. He and B. Tang, *Surf. Innovations*, 2022, **11**, 386–396.

62 Z. Wang, J. Su, H. Qi, P. Pan and M. Jiang, *Surf. Innovations*, 2020, **9**, 214–221.

63 J. Xue, Y. Zhu, M. Jiang, J. Su and Y. Liu, *Mater. Lett.*, 2015, **149**, 127–129.

64 M. Deepa, M. Kar and S. Agnihotry, *Thin Solid Films*, 2004, **468**, 32–42.

65 G. Yuan, C. Hua, L. Huang, C. Defranoux, P. Basa, Y. Liu, C. Song and G. Han, *Appl. Surf. Sci.*, 2017, **421**, 630–635.

66 H. Kim, D. Choi, K. Kim, W. Chu, D.-M. Chun and C. S. Lee, *Sol. Energy Mater. Sol. Cells*, 2018, **177**, 44–50.

67 M. Deepa, T. Saxena, D. Singh, K. Sood and S. Agnihotry, *Electrochim. Acta*, 2006, **51**, 1974–1989.

68 A. Subrahmanyam and A. Karuppasamy, *Sol. Energy Mater. Sol. Cells*, 2007, **91**, 266–274.

69 M. Deepa, A. Joshi, A. Srivastava, S. Shivaprasad and S. Agnihotry, *J. Electrochem. Soc.*, 2006, **153**, C365.

70 M. Hutchins, N. Butt, A. Topping, J. Gallego, P. Milne, D. Jeffrey and I. Brotherston, *Electrochim. Acta*, 2001, **46**, 1983–1988.

71 S. H. Lee, R. Deshpande, P. A. Parilla, K. M. Jones, B. To, A. H. Mahan and A. C. Dillon, *Adv. Mater.*, 2006, **18**, 763–766.

72 M. Yang, N. K. Shrestha and P. Schmuki, *Electrochem. Commun.*, 2009, **11**, 1908–1911.

73 Y. Yin, T. Gao, Q. Xu, G. Cao, Q. Chen, H. Zhu, C. Lan and C. Li, *J. Mater. Chem. A*, 2020, **8**, 10973–10982.

74 X. Huo, X. Miao, X. Han, S. Tang, M. Zhang and M. Guo, *J. Mater. Chem. A*, 2020, **8**, 9927–9938.

75 R. Giannuzzi, M. Balandeh, A. Mezzetti, L. Meda, P. Pattathil, G. Gigli, F. Di Fonzo and M. Manca, *Adv. Opt. Mater.*, 2015, **3**, 1614–1622.

76 Y.-T. Park, S.-H. Lee and K.-T. Lee, *Ceram. Int.*, 2020, **46**, 29052–29059.

77 S.-J. Wang, M.-C. Wang, S.-F. Chen, Y.-H. Li, T.-S. Shen, H.-Y. Bor and C.-N. Wei, *Sensors*, 2018, **18**, 2803.

78 T. Sannicolo, M. Lagrange, A. Cabos, C. Celle, J. P. Simonato and D. Bellet, *Small*, 2016, **12**, 6052–6075.

79 Y. Yao, Q. Zhao, W. Wei, Z. Chen, Y. Zhu, P. Zhang, Z. Zhang and Y. Gao, *Nano Energy*, 2020, **68**, 104350.

80 M. Bourdin, I. Mjejri, A. Rougier, C. Labrugère, T. Cardinal, Y. Messaddeq and M. Gaudon, *J. Alloys Compd.*, 2020, **823**, 153690.

81 L. Wang, Y. Liu, G. Han and H. Zhao, *J. Alloys Compd.*, 2022, **890**, 161833.

82 S. Heo, J. Kim, G. K. Ong and D. J. Milliron, *Nano Lett.*, 2017, **17**, 5756–5761.

83 C.-C. Liao, F.-R. Chen and J.-J. Kai, *Sol. Energy Mater. Sol. Cells*, 2006, **90**, 1147–1155.

84 J. Zhang, J.-p. Tu, X.-h. Xia, X.-l. Wang and C.-d. Gu, *J. Mater. Chem. C*, 2011, **21**, 5492–5498.

85 A. Al-Haddad, Z. Wang, R. Xu, H. Qi, R. Vellacheri, U. Kaiser and Y. Lei, *J. Phys. Chem. C*, 2015, **119**, 16331–16337.

86 Z. Xie, Q. Zhang, Q. Liu, J. Zhai and X. Diao, *Thin Solid Films*, 2018, **653**, 188–193.

87 A. Azam, J. Kim, J. Park, T. G. Novak, A. P. Tiwari, S. H. Song, B. Kim and S. Jeon, *Nano Lett.*, 2018, **18**, 5646–5651.

88 W. He, Y. Liu, Z. Wan and C. Jia, *RSC Adv.*, 2016, **6**, 68997–69006.

89 G. K. Mor, O. K. Varghese, M. Paulose, K. Shankar and C. A. Grimes, *Sol. Energy Mater. Sol. Cells*, 2006, **90**, 2011–2075.

90 Z. Yao, C. Wang, Y. Li and N.-Y. Kim, *Nanoscale Res. Lett.*, 2015, **10**, 1–7.

91 H.-W. Shim, Y.-H. Jin, S.-D. Seo, S.-H. Lee and D.-W. Kim, *ACS Nano*, 2011, **5**, 443–449.

92 X. Huo, H. Zhang, W. Shen, X. Miao, M. Zhang and M. Guo, *J. Mater. Chem. A*, 2019, **7**, 16867–16875.

93 D. Ma, G. Shi, H. Wang, Q. Zhang and Y. Li, *J. Mater. Chem. A*, 2013, **1**, 684–691.

94 S. Terohid, S. Heidari, A. Jafari and S. Asgary, *Appl. Phys. A*, 2018, **124**, 1–9.

95 G. Cai, J. Tu, D. Zhou, X. Wang and C. Gu, *Sol. Energy Mater. Sol. Cells*, 2014, **124**, 103–110.

96 K. Huang, Q. Zhang, F. Yang and D. He, *Nano Res.*, 2010, **3**, 281–287.

97 J.-H. Ha, P. Muralidharan and D. K. Kim, *J. Alloys Compd.*, 2009, **475**, 446–451.

98 S. Zhao, B. Wang, Y. Huang, Y. Zhang, X. Wu, Q. Jiang, D. Gao, F. Wang, R. Li and Y. Li, *ACS Appl. Nano Mater.*, 2023, **6**, 15021–15028.

99 X. Lu, G. Wang, T. Zhai, M. Yu, J. Gan, Y. Tong and Y. Li, *Nano Lett.*, 2012, **12**, 1690–1696.

100 H. Zhang, G. Li, L. An, T. Yan, X. Gao and H. Zhu, *J. Phys. Chem. C*, 2007, **111**, 6143–6148.

101 Y. Tang, Y. Zhang, J. Deng, J. Wei, H. L. Tam, B. K. Chandran, Z. Dong, Z. Chen and X. Chen, *Adv. Mater.*, 2014, **26**, 6111–6118.

102 K. Zhu, Q. Wang, J.-H. Kim, A. A. Pesaran and A. J. Frank, *J. Phys. Chem. C*, 2012, **116**, 11895–11899.

103 Y.-C. Her and C.-C. Chang, *CrystEngComm*, 2014, **16**, 5379–5386.

104 X. Xia, J. Tu, J. Zhang, X. Huang, X. Wang, W. Zhang and H. Huang, *Electrochem. Commun.*, 2009, **11**, 702–705.

105 S. Adhikari, D. Sarkar and G. Madras, *RSC Adv.*, 2015, **5**, 11895–11904.

106 X. Li, X. Song, C. Ma, Y. Cheng, D. Shen, S. Zhang, W. Liu, P. Huo and H. Wang, *ACS Appl. Nano Mater.*, 2020, **3**, 1298–1306.

107 S.-W. Baek, G. Park, J. Noh, C. Cho, C.-H. Lee, M.-K. Seo, H. Song and J.-Y. Lee, *ACS Nano*, 2014, **8**, 3302–3312.

108 Y. Lu, Y. Li, Y. Wang and J. Zhang, *Appl. Catal., B*, 2020, **272**, 118979.

109 X. Fan, T. Wang, H. Xue, B. Gao, S. Zhang, H. Gong, H. Guo, L. Song, W. Xia and J. He, *Chemelectrochem*, 2019, **6**, 543–551.

110 G. Cai, J. Tu, D. Zhou, J. Zhang, X. Wang and C. J. Gu, *Sol. Energy Mater. Sol. Cells*, 2014, **122**, 51–58.

111 X. Xia, D. Chao, X. Qi, Q. Xiong, Y. Zhang, J. Tu, H. Zhang and H. J. Fan, *Nano Lett.*, 2013, **13**, 4562–4568.

112 S. Oh, K.-M. Kang, D. Lee, S. Kim, Y.-C. Nah, S. H. Han, S. Shin, H. S. Jang and D. H. Kim, *Ceram. Int.*, 2024, **50**, 12100–12107.

113 S. A. Chambers, *Adv. Mater.*, 2010, **22**, 219–248.

114 L. Zhao, Z. Cai, X. Wang, W. Liao, S. Huang, L. Ye, J. Fang, C. Wu, H. Qiu and L. Miao, *J. Adv. Ceram.*, 2023, **12**, 634–648.

115 Y. Li, Z. Liu, L. Zhao, T. Cui, B. Wang, K. Guo and J. Han, *Electrochim. Acta*, 2015, **173**, 117–123.

116 S.-H. Yang, G.-Y. Tseng and C.-F. Kao, *J. Electrochem. Soc.*, 2019, **166**, H70.

117 Y. Xu, Q. Cao, Z. Yi, P. Wu and S. Cai, *IEEE Access*, 2020, **8**, 171350–171358.

118 Z. Bi, S. Zhang, X. Xu, X. Hu, X. Li and X. Gao, *Mater. Lett.*, 2015, **160**, 186–189.

119 Z. Bi, X. Li, Y. Chen, X. Xu, S. Zhang and Q. Zhu, *Electrochim. Acta*, 2017, **227**, 61–68.

120 R. Deshpande, S.-H. Lee, A. Mahan, P. Parilla, K. Jones, A. Norman, B. To, J. Blackburn, S. Mitra and A. Dillon, *Solid State Ionics*, 2007, **178**, 895–900.

121 Y. Zhao, X. Zhang, X. Chen, W. Li, L. Wang, F. Ren, J. Zhao, F. Endres and Y. Li, *ACS Sustainable Chem. Eng.*, 2020, **8**, 11658–11666.

122 S.-H. Yang, Z.-Y. Chen, T.-Y. Chang, P.-T. Lin and C.-C. Ho, *J. Alloys Compd.*, 2023, **965**, 171495.

123 Y. Shi, M. Sun, Y. Zhang, J. Cui, Y. Wang, X. Shu, Y. Qin, H. H. Tan, J. Liu and Y. Wu, *Sol. Energy Mater. Sol. Cells*, 2020, **212**, 110579.

124 H. Ling, L. P. Yeo, Z. Wang, X. Li, D. Mandler, S. Magdassi and A. I. Y. Tok, *J. Mater. Chem. C*, 2018, **6**, 8488–8494.

125 T. D. Nguyen, L. P. Yeo, T. C. Kei, D. Mandler, S. Magdassi and A. I. Y. Tok, *Adv. Opt. Mater.*, 2019, **7**, 1801389.

126 K. Tang, Y. Zhang, Y. Shi, J. Cui, X. Shu, Y. Wang, J. Liu, J. Wang, H. H. Tan and Y. J. Wu, *J. Mater. Chem. C*, 2018, **6**, 12206–12216.

127 Y. Shi, Y. Zhang, K. Tang, J. Cui, X. Shu, Y. Wang, J. Liu, Y. Jiang, H. H. Tan and Y. Wu, *Chem. Eng. J.*, 2019, **355**, 942–951.

128 P. Yang, P. Sun and W. Mai, *Mater. Today*, 2016, **19**, 394–402.

129 Z. Tong, Y. Tian, H. Zhang, X. Li, J. Ji, H. Qu, N. Li, J. Zhao and Y. Li, *Sci. China Chem.*, 2017, **60**, 13–37.

130 H. Li, C. J. Firby and A. Y. Elezzabi, *Joule*, 2019, **3**, 2268–2278.

131 J.-L. Wang, Y.-R. Lu, H.-H. Li, J.-W. Liu and S.-H. Yu, *J. Am. Chem. Soc.*, 2017, **139**, 9921–9926.

132 S. Cong, Y. Tian, Q. Li, Z. Zhao and F. Geng, *Adv. Mater.*, 2014, **25**, 4260–4267.

133 Z. Li, B. Wang, X. Zhao, Q. Guo and G. Nie, *New J. Chem.*, 2020, **44**, 20584–20591.

134 H. Wei, X. Yan, S. Wu, Z. Luo, S. Wei and Z. Guo, *J. Phys. Chem. C*, 2012, **116**, 25052–25064.

135 D. Ma, G. Shi, H. Wang, Q. Zhang and Y. Li, *J. Mater. Chem. A*, 2014, **2**, 13541–13549.

136 Y. Li, D. Chen and R. A. Caruso, *J. Mater. Chem. C*, 2016, **4**, 10500–10508.

137 G. Cai, D. Zhou, Q. Xiong, J. Zhang, X. Wang, C. Gu and J. Tu, *Sol. Energy Mater. Sol. Cells*, 2013, **117**, 231–238.

138 X. Huo, R. Li, J. Wang, M. Zhang and M. Guo, *Chem. Eng. J.*, 2022, **430**, 132821.

139 K. Tang, Y. Zhang, Y. Shi, J. Cui, X. Shu, Y. Wang, Y. Qin, J. Liu, H. H. Tan and Y. Wu, *Appl. Surf. Sci.*, 2019, **498**, 143796.

140 B. Zhao, S. Lu, X. Zhang, H. Wang, J. Liu and H. Yan, *Ionics*, 2016, **22**, 261–267.

141 Q. You, P. Liang, Y. Li, H. Cai, X. Yang, F. Huang, J. Sun, N. Xu and J. Wu, *Mater. Lett.*, 2015, **139**, 228–231.

142 X. Sun and J. Wang, *Nano Lett.*, 2008, **8**, 1884–1889.

143 M. Kateb, S. Safarian, M. Kolahdouz, M. Fathipour and V. J. Ahamdi, *Sol. Energy Mater. Sol. Cells*, 2016, **145**, 200–205.

144 L. Liang, J. Zhang, Y. Zhou, J. Xie, X. Zhang, M. Guan, B. Pan and Y. Xie, *Sci. Rep.*, 2013, **3**, 1936.

145 C. G. Granqvist, *Sol. Energy Mater. Sol. Cells.*, 2000, **60**, 201–262.

146 D. Dini, F. Decker and E. Masetti, *J. Appl. Electrochem.*, 1996, **26**, 647–653.

147 Y. Zhao, X. Zhang, W. Li, Z. Li, H. Zhang, M. Chen, W. Sun, Y. Xiao, J. Zhao and Y. Li, *Sol. Energy Mater. Sol. Cells*, 2022, **237**, 111564.

148 D. Di Yao, M. R. Field, A. P. O'Mullane, K. Kalantar-Zadeh and J. Z. Ou, *Nanoscale*, 2013, **5**, 10353–10359.

149 B.-R. Huang, T.-C. Lin and Y.-M. Liu, *Sol. Energy Mater. Sol. Cells*, 2015, **133**, 32–38.

150 K. Lethy, D. Beena, V. Mahadevan Pillai and V. Ganesan, *J. Appl. Phys.*, 2008, **104**, 033515.

151 Y. Meng, Z. Li and Z. Liu, *J. Mater. Sci.: Mater. Electron.*, 2022, **33**, 24995–25005.